



Final Draft of the original manuscript

Gapeeva, A.; Vogtmann, J.; Zeller-Plumhoff, B.; Beckmann, F.;
Gurka, M.; Carstensen, J.; Adlung, R.:

**Electrochemical Surface Structuring for Strong SMA Wire–
Polymer Interface Adhesion.**

In: ACS Applied Materials and Interfaces. Vol. 13 (2021) 18, 21924 –
21935.

First published online by ACS: 30.04.2021

<https://dx.doi.org/10.1021/acsami.1c00807>

Electrochemical Surface Structuring for Strong SMA Wire – Polymer Interface Adhesion

Anna Gapeeva,^{,†} Julia Vogtmann,[‡] Berit Zeller-Plumhoff,[§] Felix Beckmann,[¥] Martin Gurka,[‡]
Jürgen Carstensen,^{*,†} Rainer Adelung[†]*

[†] Functional Nanomaterials, Institute for Materials Science, Faculty of Engineering, Kiel
University, Kaiserstraße 2, D-24143 Kiel, Germany

[‡] Leibniz Institute for Composite Materials (IVW), Erwin-Schrödinger-Straße 58, D-67663
Kaiserslautern, Germany

[§] Helmholtz-Zentrum Geesthacht, Institute of Metallic Biomaterials, Max-Planck-Straße 1, D-
21502 Geesthacht, Germany

[¥] Helmholtz-Zentrum Geesthacht, Institute of Materials Physics, Max-Planck-Straße 1, D-21502
Geesthacht, Germany

KEYWORDS

NiTi SMA wire, hybrid composite, electrochemical etching, surface structuring, interface
adhesion, force transmission, pull-out, optical stress measurement

ABSTRACT

Active hybrid composites represent a novel class of smart materials used to design morphing surfaces, opening up new applications in the aircraft and automotive industries. The bending of the active hybrid composite is induced by the contraction of electrically activated shape memory alloy (SMA) wires, which are placed with an offset to the neutral axis of the composite. Thereby the adhesion strength between the SMA wire and the surrounding polymer matrix is crucial to the load transfer and the functionality of the composite. Thus, the interface adhesion strength is of great importance for the performance and the actuation potential of active hybrid composites. In this work, the surface of a commercially available one-way effect NiTi SMA wire with a diameter of 1 mm was structured by the selective electrochemical etching that preferably starts at defect sites, leaving the most thermodynamically stable surfaces of the wire intact. Created etch pits lead to an increase in surface area of the wire and a mechanical interlocking with the polymer, resulting in a combination of adhesive and cohesive failure modes after a pull-out test. Consequently, the force of the first failure determined by an optical stress measurement was increased by more than three times when compared to the as-delivered SMA wire. The actuation characterization test showed that approximately the same work capacity could be retrieved from structured SMA wires. Moreover, structured SMA wires exhibited the same shape of the stress-strain curve as the as-delivered SMA wire, and the mechanical performance was not influenced by the structuring process. The austenite start A_s and austenite finish A_f transformation temperatures were also not found to be affected by the structuring process. The formation of etching pits with different geometry and density was discussed with regard to the kinetics of oxide formation and dissolution.

1. INTRODUCTION

As a result of the continual increase in demand for materials with respect to weight, flexibility, and strength, conventional materials are often no longer sufficient. Smart materials such as active hybrid composites produced from NiTi shape memory alloy (SMA) wires and fiber-reinforced polymers (FRP) represent a novel class of materials that opens up new functionalities and application possibilities.^{1,2} In general, SMA materials are characterized by their ability to exhibit a mechanical response when subjected to a thermal field.³ Thus, by embedding an SMA wire in a thin-walled FRP, a tailored shape-changing, or morphing, surface can be designed. The elimination of the need for an additional mechanical actuation makes active hybrid composites highly attractive for actuator applications in the aircraft and automotive industry since substantial savings regarding weight, space, and cost can be achieved.⁴⁻⁷

Compared to other actuation technologies such as, for example, piezoceramics, SMAs exhibit an outstanding volumetric energy density, defined as work output per unit volume. They can provide actuation stresses up to 600 MPa accompanied by large recoverable strains up to 6 %, with the only limitation being the operating frequency.³ Therefore, when combined with an elastic matrix, e.g., FRP, which acts as a tailored antagonistic partner in cyclic actuation, new applications such as vortex generators, winglets, or wing airfoils are possible.^{4,8} The bending of the active hybrid composite is induced by a contraction of an activated SMA wire positioned with an offset to the neutral axis of the composite.⁵ In addition to the internal stress resulting from the shape change, the hybrid composite often has to work against an external force (e.g., caused by the airflow in aerodynamic applications). Thus, the force transmission at every point along the axis between the SMA wire and the surrounding polymer matrix is crucial to achieving

bending with a predefined shape with no gaps and kinks. Since the first failure of the composite usually occurs at the interface between the SMA wire and the polymer matrix, the interface strength is often a limiting factor for the actuation potential and restricts the application range. After the interface failure, no force transmission between the SMA wire and the polymer matrix is possible. Hence, it is of utmost importance to understand the stress transfer and distribution mechanisms as well as the limiting factors at the interface to improve the adhesion between the SMA wire and the polymer matrix.^{9,10}

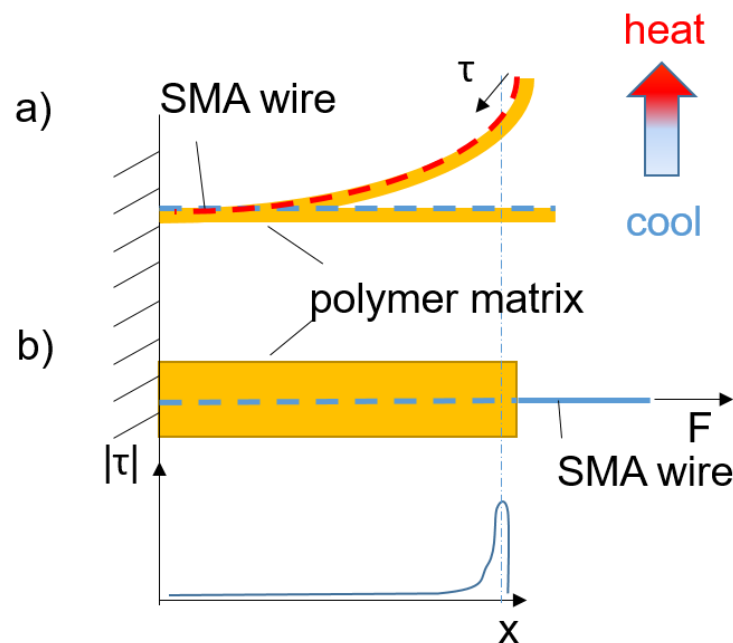


Figure 1. Schematic illustration of an active hybrid composite and shear stress distribution: a) during the activation process, b) during the pull-out test. In both cases, the maximum shear stress at the interface occurs in the outer area of a hybrid composite. SMA wire is shown in the initial non-activated (cooled) and activated (heated) states in blue and red, respectively.

The total amount of the shear stress at the interface during the bending of the hybrid composite is highly dependent on the position along the length of the SMA wire (Figure 1). The critical areas in terms of achieving the maximum actuation performance of the SMA wire in the surrounding polymer matrix are the outer areas of the hybrid composite in which the maximum shear stress τ is concentrated.^{2,9} Once the critical stress value in this area is exceeded, the debonding process will begin.⁹ Interface strength, i.e., the stress transfer between an SMA wire and a polymer matrix, is usually evaluated by measuring the maximum shear stress τ in the pull-out test.¹¹⁻¹³ Additionally, the force at first failure can be identified using the optical stress measurement.^{9,14}

Standard methods to improve adhesion between an SMA wire and a polymer matrix involve modifications of a metal surface by mechanical, physical, and chemical means or a combination thereof. Application of abrasive mechanical treatments such as handsanding or sandblasting^{9,11,15} as well as physical patterning of the surface by laser¹⁶ aim to increase the surface roughness that results in mechanical coupling effects (interlocking). Mechanical coupling can also be achieved by introducing crimp sleeves, spot-welded anchor wires,⁹ or by twisting the SMA wires themselves.¹⁷ Adhesion promotion by chemical treatments, on the other hand, relies on the introduction of new functional groups or compounds at the interface (often requiring removal of the native oxide layer and controlled passivation in the first step), providing for a chemical bond between the two materials. Several authors investigated the use of silane¹⁸⁻²¹ and other chemical coupling agents/conversion coatings²²⁻²⁴ to increase the bonding strength between the SMA wire surface and the polymer matrix. However, industrially-applicable adhesion promoters such as chromate-based primers are of considerable concern regarding their toxicity and carcinogenic hazard.^{25,26}

Our approach has decisive differences compared to the methods mentioned above:

- The structuring process is selective to crystal defects and impurities. The etched surface is thus composed of the most thermodynamically stable surfaces. In contrast, in the case of mechanical/physical roughening treatments, the material is removed from the surface regardless of its quality, which leads to surface deterioration.
- No harsh chemicals are required for the process, in contrast to the application of chemical adhesion promoters.

The surface structuring, which significantly improves adhesion between metal (e.g., Al, Zn, Ti, steel) surfaces and various polymers under mechanical load, can be done either chemically or electrochemically, as was shown in the previous publications from our group.²⁷⁻³⁰ Other research groups have already attempted to apply chemical etching to SMA surfaces to increase the interface adhesion.^{15,31-35} Thereby, the SMA surface was immersed into an aqueous acidic solution containing HCl, HNO₃, H₂SO₄, and/or HF, while the treatment time varied from minutes to several hours. Generally, an improvement of the interface adhesion was observed and attributed to an increased surface roughness of the SMA wire.³¹ However, only a few publications addressed the influence of acid treatments on the mechanical properties of SMA and reported a reduction of tensile strength³⁴ as well as embrittlement even after short immersion times due to hydrogen absorption.³⁶

Compared to chemical etching, the electrochemical etching process applied in this work brings advantages in terms of time efficiency (the total treatment time per SMA wire in this work was less than half a minute) and reduced susceptibility to hydrogen embrittlement. The latter results from the short treatment time and the experimental setup, in which the SMA wire is connected to

the positive pole, and positively charged hydrogen ions are thus pushed away from the treated surface. So far, electrochemical treatments were mostly applied to increase corrosion resistance and biocompatibility of NiTi SMA surfaces for biomedical applications³⁷⁻⁴⁰ or the fabrication of microactuators from SMA sheets.^{41,42} Some sporadic attempts have been made to use electrochemical treatments to improve the interface adhesion, but these were mainly based on anodizing^{12,43,44}, which typically leads to a formation of a thick rough oxide layer on the surface. In our approach, the dissolution and oxide formation rates are balanced, allowing us to control the surface topography and chemical composition of the surface, as a result of which the metal surface is covered only with a very thin unavoidable oxide layer. Along with a pull-out test and optical stress measurement to determine the force of the first failure, a thorough characterization of mechanical and thermomechanical properties of structured SMA wires was performed.

2. MATERIALS & METHODS

2.1. SMA Wire

All experiments were carried out with a commercially available one-way effect NiTi SMA wire (Alloy H) from Memry Corporation (Bethel, USA) with a nominal diameter of 1 mm, Ni content of 55.09 wt%, and a transition temperature for the thermoelastic phase transition from the martensite to austenite phase of A_s 70 °C. The black oxide layer forming during heat treatments and training of NiTi SMA wire was removed by the manufacturer. Before each experiment, the SMA wires were heat-treated for 15 minutes at 100 °C to avoid the influence of residual stress caused by the storage or the manufacturing process. The SMA wires were then allowed to cool down to room temperature (RT) and transform back to the martensitic state.

2.2. Matrix Material

The cold-curing epoxy resin used as a polymer matrix material was purchased from Huntsman Corporation (The Woodlands, USA). A formulation of 100 g Araldite[®] LY 5052 and 38 g

Aradur® 5052 was manually mixed for 2 minutes at RT. To ensure a void-free polymer matrix, the hybrid composite was cured for 2 days in the autoclave under predefined conditions (2 bar at RT) and afterwards for 5 days under atmospheric pressure at RT. The material data of the used epoxy provided by the manufacturer⁴⁵ as well as the shear modulus calculated* according to Ehrenstein⁴⁶ are summarized in Table 1.

Table 1. Material data of the used epoxy matrix.

Curing time	Tensile modulus	Shear modulus*	Fracture energy	Glass transition temperature
7 days at RT	3350 MPa	1240.74 MPa	0.19 N/mm	60 °C

The choice of the polymer matrix resin is based on a thorough consideration of many parameters such as viscosity and wetting behavior during processing, as well as stiffness and strength of the cured polymer matrix. Due to the difference in the glass transition temperature of the polymer matrix (60 °C) and the activation temperature of the SMA wire (70 °C), post-curing effects during activation have to be taken into account. However, it has been shown that when tested at room temperature, no significant difference in the force of the first failure during a pull-out experiment was found between samples with and without additional post-curing. Moreover, when the experiment was conducted at an elevated temperature (100 °C), an increase in the force of the first failure force was observed.⁹

2.3. Electrochemical Etching

The in-house-built electrochemical etching setup used in this work comprises an etching cell connected to a DC voltage source, electrolyte container, and a peristaltic pump (Figure 2). The SMA wire placed inside the etching cell is designated as a working electrode (WE), or anode, and is connected to the positive pole of the DC voltage source while a metallic (stainless steel)

counter electrode (CE), or cathode, surrounding the SMA wire is connected to the negative pole. The etching process only starts when a DC voltage between the WE and CE is applied. The etching is driven in a galvanostatic mode, i.e., the current (density) flow is controlled as a function of etching time. The necessary current is calculated from the desired current density and the surface area of the SMA wire to be etched. In this study, the etching length of all samples was 10 cm. Three morphologically different structures were obtained by etching in two steps: 1) nucleation at high current densities, 2) selective etching at lower current densities while the applied current is either pulsed (structures 1 and 2) or constant (structure 3). The etching parameters are summarized in Table 2. The electrolyte, which consists of a 4.4 wt % NaCl and 0.26 wt % HCl, is continuously pumped through the etching cell by a peristaltic pump with a constant flow rate of 1.4 l/min.

Table 2. Electrochemical etching parameters.

Structure	Nucleation		Selective etching			
	Duration	Current density	Pulse duration		Pulse current density	No. of pulses
			Current OFF	Current ON		
1	0.25 s	8 A/cm ²	3 s	5 s	1 A/cm ²	3
2	0.25 s	10 A/cm ²	3 s	1 s	2.5 A/cm ²	6
3	0.25 s	10 A/cm ²	-	6 s	2.5 A/cm ²	-

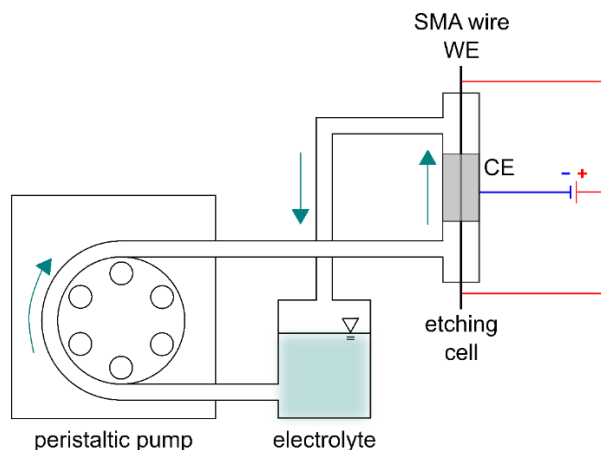


Figure 2. Electrochemical etching setup.

2.4. Surface Characterization

2.4.1. SEM/EDX

Surface morphology investigations were conducted using the ZEISS ULTRA PLUS scanning electron microscope (SEM) with the GEMINI column (Carl Zeiss Microscopy GmbH, Jena, Germany) equipped with an Energy-dispersive X-ray (EDX) analysis system from Oxford Instruments. Chemical composition analysis by means of EDX was performed at the accelerating voltage of 15 kV. To analyze the SMA wires after the pull-out test, the SMA wires were sputtered with a thin layer (< 10 nm) of gold-palladium.

2.4.2. Micro-Computed Tomography (Micro-CT)

Three SMA wires (structure 1-3) etched according to parameters summarized in Table 2 were imaged at the high-energy materials science (HEMS) beamline P07 at the PETRA III storage ring, operated by Helmholtz-Zentrum Geesthacht at Deutsches Elektronen-Synchrotron (DESY). A photon energy of 55.75 keV was selected, and imaging was performed around 360° with 4800 projections. The 3D reconstruction was conducted with three times binning of raw images, resulting in an isotropic voxel size of 0.673 μm . After reconstruction, the images were filtered using a 3D median filter with a 2x2x2 kernel size. Image segmentation was then performed using

the trainable WEKA segmentation tool.⁴⁷ Avizo[®] 9.4.0 (FEI SAS, Thermo Scientific[™], France) was used to determine the convex hull of the SMA wire, to align it along its long axis, and to identify the etch pits. To separate the erroneously connected pits, the BoneJ thickness plugin⁴⁸ in Fiji ImageJ⁴⁹ was used to determine the dimensions of the pits, whereby all pits smaller than 15 voxels were excluded (for details, see Supporting Information S1). Avizo was then utilized to determine the volume, the surface area, and centroids of the remaining pits. The etching depth was calculated as the maximum sphere fitting into each pit, as determined by the BoneJ plugin. The aligned image volume was exported and further processed in Matlab[®] R2019b (The MathWorks[®] Inc., USA). The distances of the ten nearest neighbor pits were calculated based on the pit centroids as determined by Avizo. For the data analysis, the same cylindrical sample volume with a height of 1.117 mm and a diameter of approx. 1 mm was considered for all three samples. To verify whether the determined etch pit parameters are statistically significantly different, a one-way ANOVA test was conducted using Matlab.

2.5. Mechanical and Shape Memory Properties

2.5.1. Pre-Strain and Tensile Test

Both tests (pre-straining and tensile test) were performed with the universal testing device Zwick RetroLine (ZwickRoell GmbH & Co. KG, Ulm, Germany) with a 10 kN load cell. The pre-straining of the SMA wires was performed at a test speed of 500 mm/min until 4.5 % strain was reached with a clamping length of 90 mm at the beginning. The tensile test was carried out with the same clamping length but at a test speed of 400 %/min, which was set by experience.

Thereby the aim was to achieve the detwinning process of the SMA lattice structure as homogeneous as possible by rapid pulling. The tensioning of the SMA wires in the testing device was done using pneumatic clamps (2 bar). For the pre-strain test, a minimum amount of 10 samples per wire configuration was used, while for the tensile test, 5 samples per wire

configuration were tested. The test data were analyzed using open-source routines written in Python[®] 3.7 (pandas, numpy, matplotlib, scipy stats). The stress for as-delivered and structured SMA wire configurations was calculated with respect to the cross-sectional area determined by micro-CT. Additionally, the corresponding 99 % confidence intervals were calculated for each measurement point of each SMA wire configuration.

2.5.2. Actuator Characterization Setup

A custom-made test setup was used to characterize the actuation potential of the different SMA wire configurations. Thereby pre-strained SMA wires were working against a leaf spring with an adjustable length and 29 N/mm stiffness. The SMA wires were activated by electric current (0 A to 6 A). The temperature in the tested SMA wire due to applied electric current was recorded via a thermal camera (TIM 160, Micro-Epsilon Messtechnik GmbH & Co. KG, Ortenburg, Germany). The resulting actuation force of the SMA wire, working against the leaf spring was measured by a load cell (1 kN, HBM, Hottinger Brüel & Kjaer GmbH, Darmstadt, Germany) while the achieved strain was measured by a laser sensor (optoNCDT, Micro-Epsilon Messtechnik GmbH & Co. KG). The SMA wire was heated from RT to approx. 145 °C with a heating rate of approx. 4.8 K/s, the clamping start length was 90 mm. The test principle is explained in more detail in previous research.⁸ The test was finished after a defined time interval without temperature change was measured. Due to the complexity and time dependence of the test, only one SMA wire of each configuration was measured. The test results were evaluated using Python[®] 3.7 (numpy, matplotlib, re, mtah, pylab).

2.5.3. Dynamic-Mechanical-Thermal-Analysis (DMTA)

DMTA was performed using the TA Instruments DMA 850 (TA Instruments, Inc., New Castle, USA) with the constant stress of 0.1 MPa and variable strain. The temperature was increased from 20 °C to 150 °C with a heating rate of 2 K/min. The starting length of all tested SMA wires

was 15 mm. 4 pre-strained SMA wires of each configuration were tested. The transformation temperatures A_s and A_f were determined using the TA instruments software TRIOS and Python[®] 3.7 (pandas, numpy, matplotlib).

2.6. Pull-Out Test

In order to induce a similar stress state in all SMA wire configurations and to ensure the comparability of the results, the mechanically induced pull-out test was performed, which corresponds to the state of the art.^{24,34,35,50} In the case of the thermally activated pull-out test, the stress distribution at the interface has not yet been understood since the transformation behavior, and thus, the contraction of the SMA wire is not homogeneous.^{9,51}

2.6.1. Pull-Out Test Sample Preparation

SMA wires were embedded in the polymer matrix using a custom-made mold, consisting of a silicone mold and a one-side open steel frame, as shown in Figure 3. First, the polymer matrix was filled into the silicone mold. To allow for precise positioning of the SMA wires in the polymer matrix and to avoid lateral stresses during the test, the SMA wires were then clamped in the steel frame. The samples were cured, as described in 2.2. After curing, the samples were cut to obtain samples with a defined size (H x B x T) of 50 mm x 18 mm x 9 mm. The embedded SMA wire length was 50 mm.

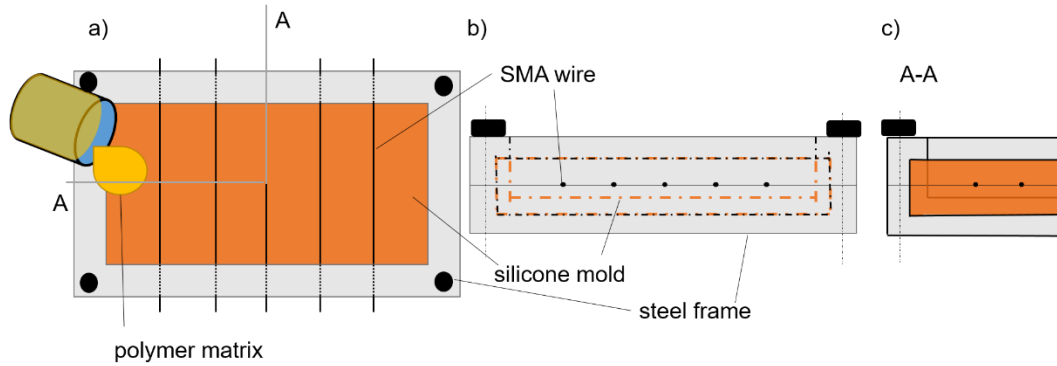


Figure 3. Sample preparation for the pull-out test: a) top view, b) front view, and c) A-A cross-sectional view. To ensure precise positioning of SMA wires inside the polymer matrix, the SMA wires were fixed using a one-side open steel frame, through which the polymer was filled in.

2.6.2. Pull-Out Test Setup

The pull-out test was performed at RT using the universal testing device setup for tensile testing Zwick RetroLine with a 10 kN load cell and a preload of 5 N at a strain-rate of 25 %/min, which corresponds to the activation speed of a typical SMA wire. Figure 4 shows the custom-made sample holder, clamped in the lower clamping jaw of the tensile test device, which was designed to allow precise positioning of the samples to avoid lateral forces and stress concentrations due to clamping. The free end of the SMA wire was fixed with pneumatic clamps (2 bar) in the upper clamping jaw. During the pull-out test, the pull-out force was applied directly to the SMA wire. The free length of the tested SMA wires was 40 mm. To clearly identify the force of the first failure, which cannot be directly derived from a force-displacement curve,⁹ the pull-out test was accompanied by optical stress measurement based on photoelasticity. Thereby a linear polarizer setup and an ultrahigh-speed camera Motion v2512 (Vision Research, Wayne, USA) with a framerate of 1000 frames per second were used. The data analysis was carried out using a system of Stemmer Imaging AG (Puchheim, Germany). The correlation between the force-time curve measured by the universal testing device and the stress at the interface recorded optically

was done using a script of a self-written GUI environment in Python[®] 3.7 (numpy, matplotlib, pandas, xlrs, padoc, ipython, ipykernel, opencv). The script automatically compensated for the difference in the recording frequency between the ultrahigh-speed camera and the material test device. At least 5 samples were tested for every configuration. Additionally, the Nalimov outlier test⁵² was used.

The maximum transferable shear stress was calculated according to an analytical model.⁵³ (for details, see Supporting Information S2).

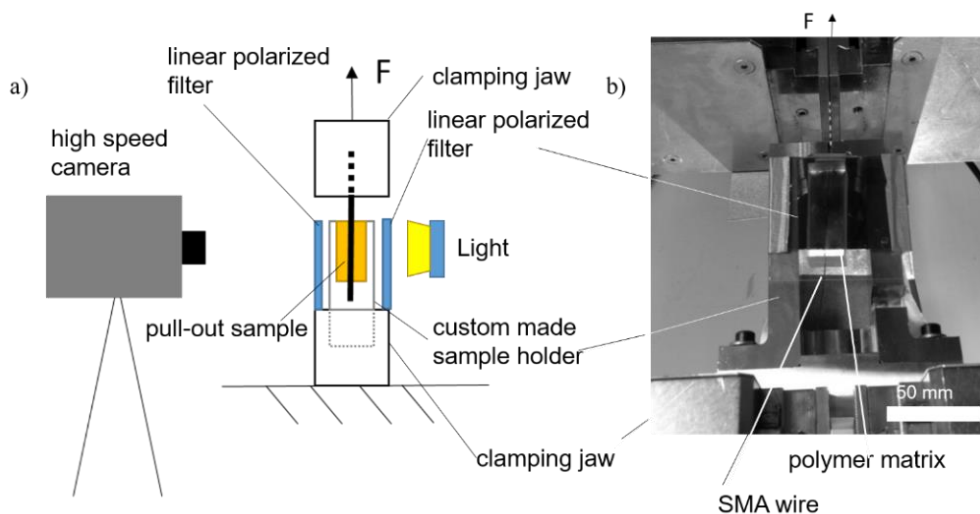


Figure 4. Schematic illustration of the pull-out test setup: a) full setup side view, b) detailed front view, showing a pull-out sample in the custom-made sample holder. The force is applied directly to the SMA wire, while the polymer matrix is held by the custom-made sample holder.

3. RESULTS AND DISCUSSION

3.1. Surface Morphology and Composition

SEM examination of the surface allows for a first qualitative evaluation of the microstructure morphologies resulting from etching with different parameters. From Figure 5a, one can observe that etching with longer and weaker pulses (structure 1) leads to wide and spatially distributed

pits. In contrast, shorter and stronger pulses (structure 2) result in smaller but more densely distributed pits. Application of a constant current (structure 3), on the other hand, causes the etch pits to widen and finally to overlap. From these results, it becomes apparent that dissolution reactions alone (which are the same for all three structures) are not sufficient to explain the differences in the formation of the created structures, so that the kinetics of oxide formation and dissolution has to be considered in more detail.

Electrochemical structuring of metal and semiconductor surfaces is a highly nonlinear process that will not be explicitly discussed here. Instead, some more general issues will be explained, which allow us to understand the parameter dependencies for the etching results found in this study. Due to the high activity of Ti (standard reduction potential $E^0 = -1.6$ V),⁵⁴ Ti atoms (in direct contact to the electrolyte) dissolve easily and form oxides without any additional electrochemical driving forces. On the other hand, a native TiO₂ layer covering the surface of NiTi is stable against chemical dissolution by Cl⁻ ions⁵⁵ and cannot be chemically dissolved by our low concentrated electrolyte. Besides, an insulating TiO₂ layer cannot be etched by an electrochemical equilibrium reaction governed by the Nernst equation because no significant potential can be applied to the Helmholtz layers. The (full) applied potential will drop across the TiO₂ layer, inducing high electrical fields that give rise to local electrical breakthroughs.⁵⁶ Therefore, it is rather a heat and mechanical force driven process that locally cracks the TiO₂ layer and brings pure metallic Ti in direct contact with the electrolyte. The cracking is most likely to occur at sites where the quality of the passivation layer is worse due to underlying crystal defects, impurities, or local roughness peaks. The following strong Ti dissolution will widen the breakthrough gap by etching underneath the oxide and thus induce positive feedback for further Ti dissolution. Reaction products and educts now start to accumulate at the interface,

hindering a further Ti dissolution, supporting the formation of TiO₂ and subsequent coverage of the surface with a closed TiO₂ layer. Thus, Ti dissolution consists of sequences of several self-amplifying and self-suppressing processes that induce a lateral coupling to neighboring surface areas and open a wide field for nonlinear collective phenomena, which all show time-critical kinetic effects. Depending on the rate of formation and dissolution of the passivation layer, some spots are, therefore, more easily etched, such as defect-rich phases with higher energy levels compared to undistorted areas. Once started, the current will be carried preferably at the existing pits that will grow mostly sideways due to the higher energy levels of the atoms at the pit edges where most of the bonds are broken. This mechanism explains the lateral extension and overlapping of pits in the case of structure 3, where pits were first nucleated at a higher current density (10 A/cm²) and then allowed to grow at a lower constant current density (2.5 A/cm²). However, by pulsing the current (after the nucleation step), it is possible to restrain the dissolution and to enhance the etching selectivity. The introduction of pause times allows areas with a good crystalline structure and better access to passivating species to passivate faster than defect-rich and depleted areas. Thereby it can be distinguished between flat surfaces and already existing pits (e.g., after the nucleation step) as well as areas with different crystalline structures inside the pits. In order for pits to grow in depth, the current pulse width and amplitude has to be chosen in that way that the difference in kinetics of oxide formation between flat surfaces and surfaces inside pits is at maximum, i.e., the flat surfaces have enough time to passivate while the extent of passivation of surfaces inside the pit is lowest. Then, when the current is on, it will be more likely to start inside the pit than on a flat surface. Due to crystal inhomogeneities inside the pit, the etching may result in the formation of undercut structures. Investigation of a cross-section by means of micro-CT confirms the presence of omega-like pits (Figure 5b). By applying

short pulses (1 s) at a higher current density (2.5 A/cm²), as in the case of structure 2, the concentration of passivating species is locally decreased each time the current is switched on, leading to an increase of diffusion limitation and a higher number of pits growing in depth. In the case of structure 1 with weaker (1 A/cm²) but longer (5 s) pulses, fewer of the nucleated pits are activated, but instead, these are growing in depth and volume. These conclusions are in good agreement with the analysis of data obtained by micro-CT (Figure 5b,c), showing significant differences ($p < 0.01$) between the etch pit parameters of different structures: in the case of structure 1, the distributions of the etch pit size (Figure 6a) and etch pit volume (Figure 6c) show two local peaks indicating that there are two populations of etch pits, i.e., short-lived (extinct after nucleation) and long-lived (continuing to grow) pits. Structure 2, on the other hand, shows steeper unimodal distributions with its single peaks shifted to the left, confirming that there is a higher number of smaller long-lived pits compared to structure 1. Results from the examination of ten nearest neighbor distances in Figure 6b clearly show a higher etch pit density of structure 2, the distribution of which is shifted towards shorter distance values compared to structure 1. Finally, Figure 6d illustrates the distribution of the etch pit depth, where structure 1 exhibits the deepest and structure 3, as expected, the shallowest etch pits, whereas structure 2 is in between.

Examination of the surface composition by EDX reveals that the etching process leads to a decrease of the Ni content compared to the as-delivered surface (Table 3). The descending amount of Ni from structure 1 to structure 3 can be attributed to the difference in etch pit depth and, thus, the different signal strength from the etched surfaces. In Figure 7, the as-delivered surface of the SMA and the surface after etching (structure 3) with corresponding element maps are shown. It can be observed that the distribution of Ni and Ti on the untreated surface is homogeneous, whereas for the etched surface, the Ti distribution remains uniform, and the

etched areas are depleted in Ni. This indicates that our electrochemical etching is selective with respect to Ni. While the thin native TiO₂ layer covering the untreated SMA surface cannot be detected by EDX, the oxide which is forming at the etched sites is thicker due to the nonlinear dynamics of its formation and dissolution as well as the roughness of the underlying surface that results in a strong O signal for the etched surface.

Table 3. Element composition from EDX analysis.

SMA wire	as-delivered	structure 1	structure 2	structure 3
Ni:Ti ratio	1.21	0.98	0.93	0.88

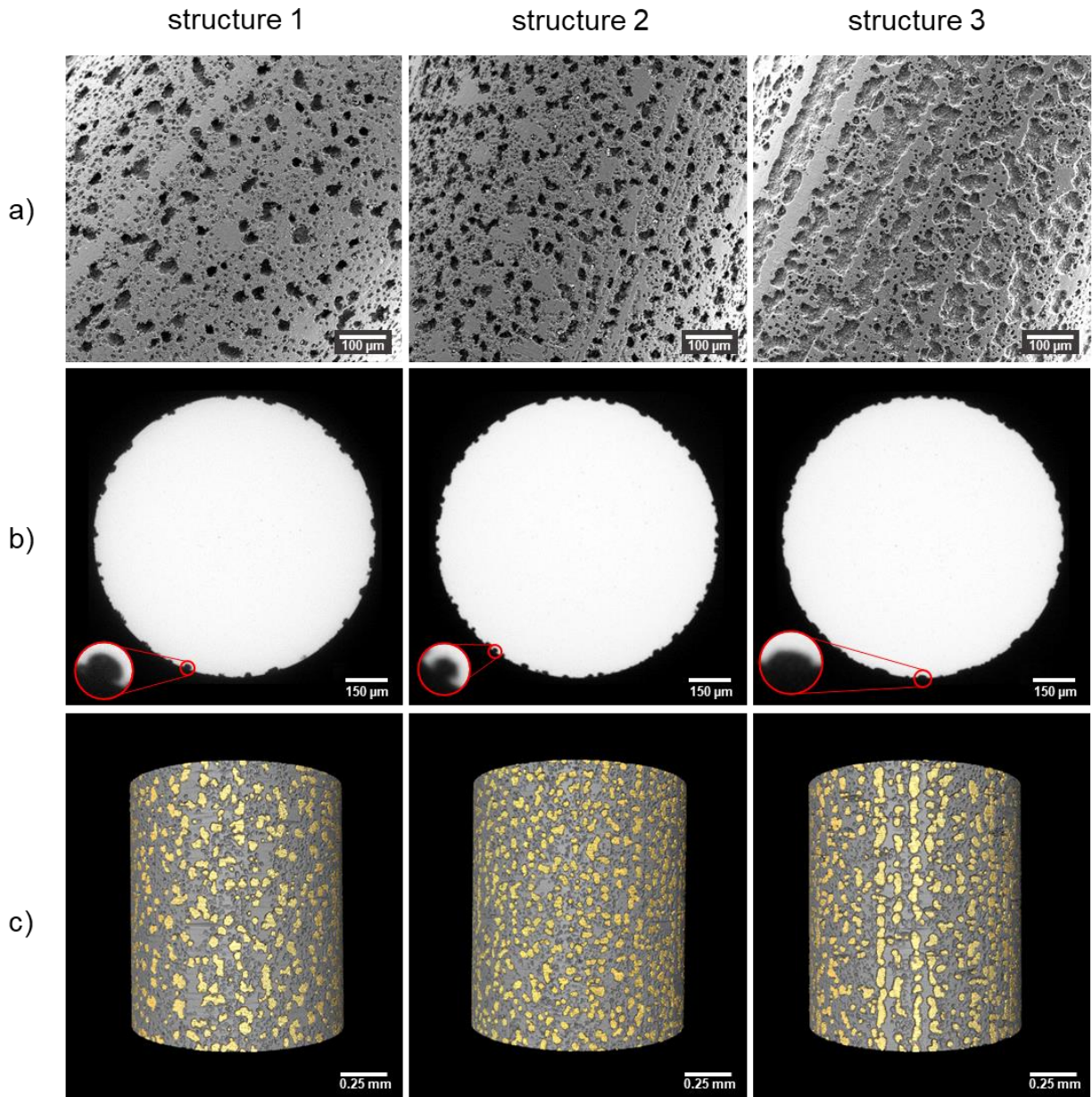


Figure 5. a) SEM micrographs of the electrochemically structured SMA wire surfaces, b) exemplary image slices of micro-CT scans, c) 3D renderings of reconstructed micro-CT volumes with identified etch pits.

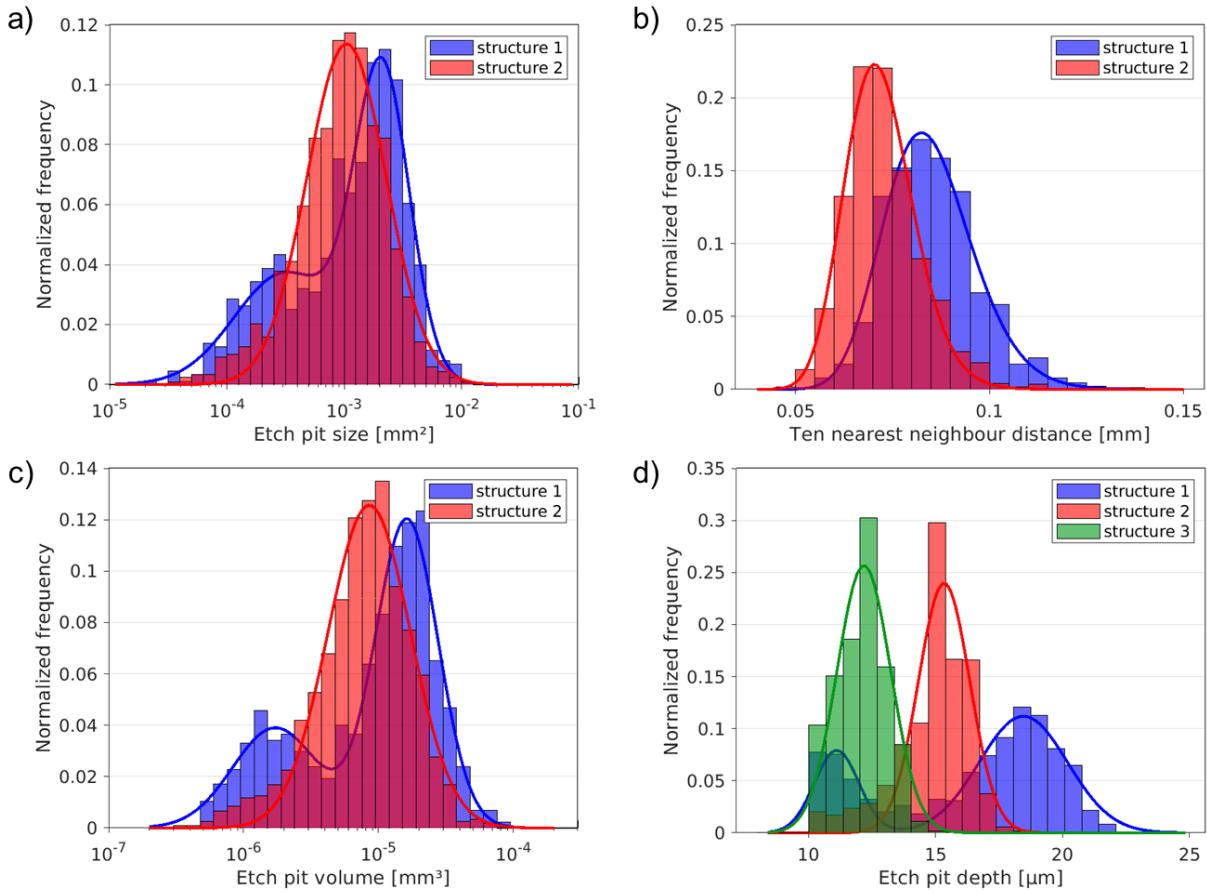


Figure 6. Micro-CT data analysis of electrochemically structured SMA wires, showing normalized distributions of different etch pit characteristics. Distributions of a) etch pit size, b) ten nearest neighbour distance, and c) etch pit volume illustrate the differences in etch pit characteristics of structures produced with pulsed current (structures 1 and 2), while the distribution of d) etch pit depth illustrates that the lowest etching depth is produced at constant current (structure 3).

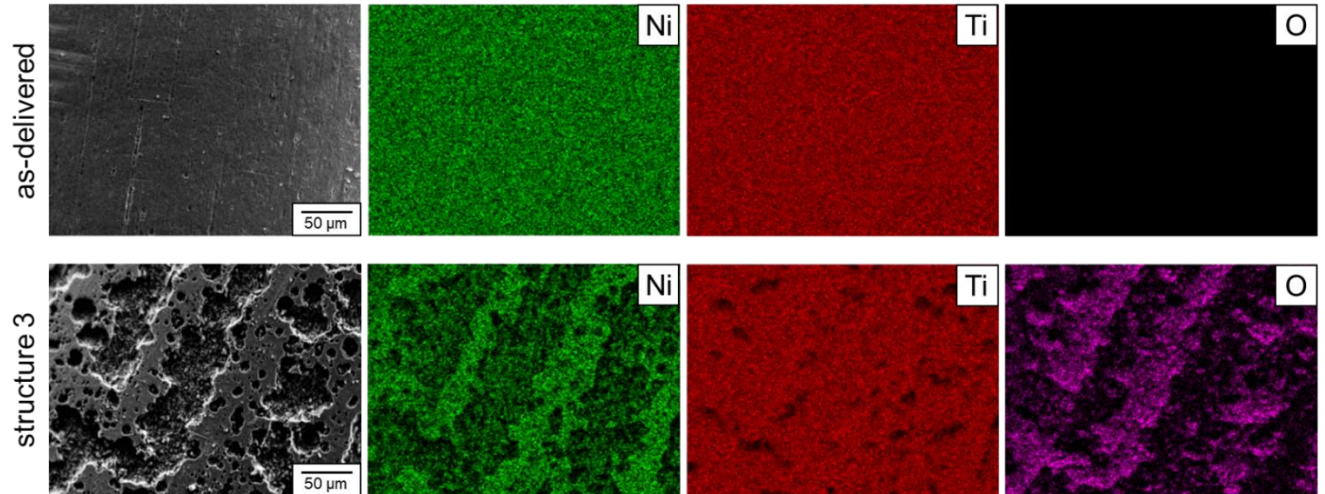


Figure 7. SEM micrographs and corresponding EDX element maps of an as-delivered wire and an etched wire with structure 3.

3.2 Mechanical and Shape Memory Properties

3.2.1. Pre-Strain and Tensile Test

The stress-strain diagram generated by pre-straining the different SMA wire configurations is presented in Figure 8a). All SMA wire configurations showed stress-strain characteristics that are typical for the chosen SMA wire, namely two plateaus associated with the R-phase for small strains below 0.56 % and the martensite detwinning from 1.1 to 4.5 %. The average ultimate stress values of $139.1 \text{ MPa} \pm 1.8 \text{ MPa}$, $136.2 \text{ MPa} \pm 2.2 \text{ MPa}$, $137 \pm 2.6 \text{ MPa}$, and $138.3 \pm 2.1 \text{ MPa}$ were found for the as-delivered, structure 1, structure 2, and structure 3 SMA wires, respectively. Considering the calculated 99 % confidence intervals, the structured SMA wire configurations showed no significant reduction in stress values compared to the as-delivered state.

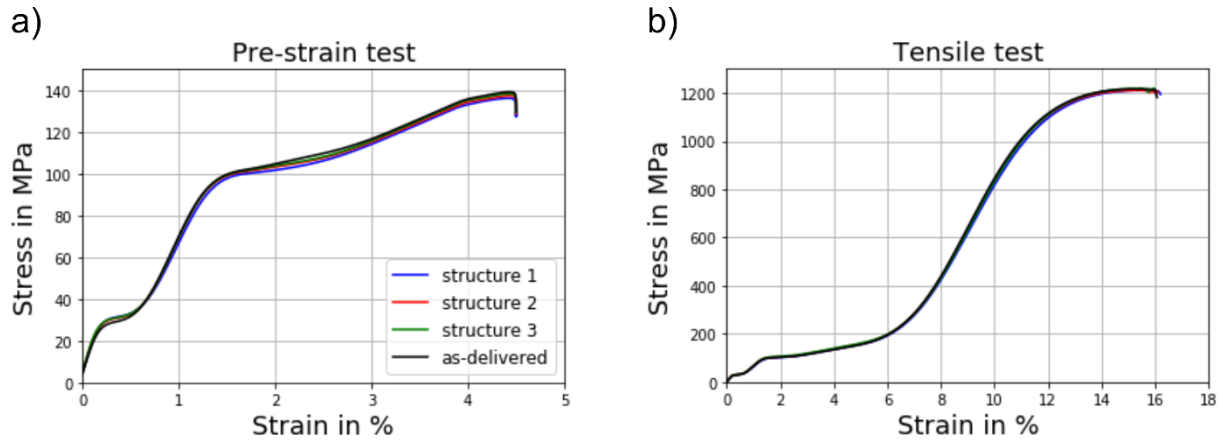


Figure 8. Stress-strain diagrams obtained from a) the pre-strain test, b) the tensile test. The curves represent the average stress values for all SMA wire configurations (for detailed views with the corresponding 99 % confidence intervals s. Supporting Figure S2).

The tensile test shows similar stress-strain characteristics as the pre-strain test, with an additional elastic region of the completely detwinned martensite starting at approx. 6 % strain (Figure 8b). All structured SMA wires exhibited the same shape of the stress-strain curve as the as-delivered SMA wire, indicating that the etching procedure provides a reproducible and homogeneous structuring along the length of the SMA wire (additionally, a reproducibility test is shown in Supporting Information S4). The calculated average value of the ultimate tensile strength for the as-delivered wire was $1217.6 \text{ MPa} \pm 4.9 \text{ MPa}$, while the for the structured SMA wires configurations it amounted to $1210.7 \text{ MPa} \pm 3.06 \text{ MPa}$, $1211.0 \pm 1.44 \text{ MPa}$, and $1217.8 \pm 2.57 \text{ MPa}$ for structure 1, structure 2, and structure 3, respectively. Overall, considering the calculated 99 % confidence intervals, no significant reduction in the mechanical performance of structured SMA wires was observed.

3.2.2. Characterization of the Actuation Behavior

The actuation capability of the SMA wires is demonstrated as actuation stress vs. actuation strain diagram in Figure 9. Thereby the SMA wire is heated above the transformation temperature (A_f)

and is working against a spring. Since the SMA wire contracts during actuation, the strain is plotted on the negative axis. After reaching the maximum test temperature, the current is switched off, and the SMA wire cools down to ambient temperature due to air convection. Since the SMA wires used in this study are one-way effect wires, the reverse shape change during cooling (Figure 9b) is induced only by the restoring force of the spring. However, the stiffness of the spring is not sufficient to recover the previously retrieved strain, i.e., to pre-strain the SMA wires up to 0 %. Different strain values achieved during cooling by the as-delivered wire and etched configurations are due to the shutdown criteria of the setup explained in more detail in Supporting Information S5.

The as-delivered SMA wire showed the maximum actuation stress at 122.2 MPa and the maximum actuation strain of -2.265 %, which corresponds to the work capacity of 0.255 J. Compared with the work capacity introduced by the pre-straining (0.455 J), 56 % of the maximum possible work capacity was retrieved from the as-delivered SMA wire. From the structured SMA wire configurations, structure 2 showed the highest retrieved work capacity of 58 %, followed by structure 3 (57.3 %) and structure 1 (53.3 %). Since only one SMA wire of each configuration was measured, no trend regarding the differences between the differently structured SMA wires can be derived, but the obtained values indicate that SMA wires' actuation performance was not impaired by the electrochemical structuring process.

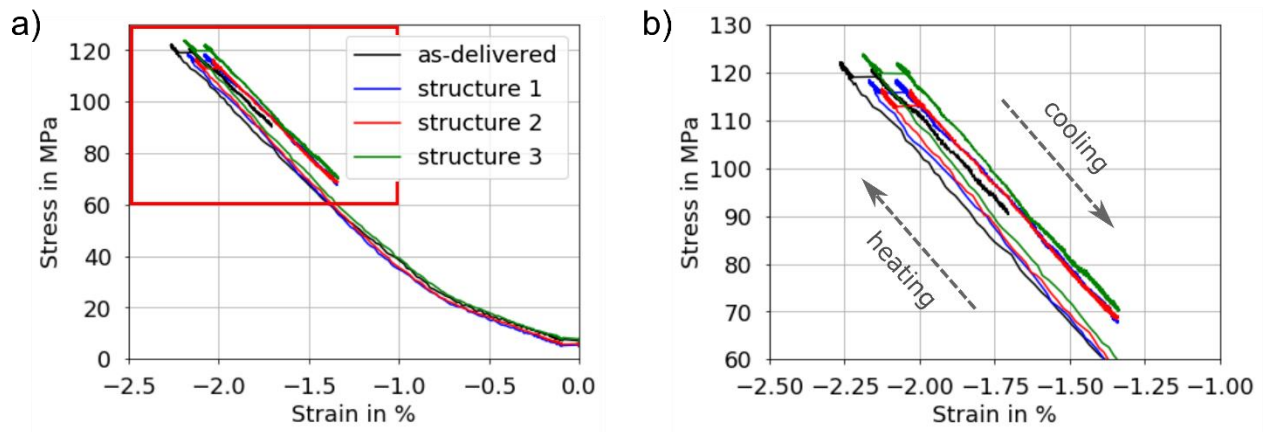


Figure 9. Actuation behavior of the different SMA wire configurations working against a spring: a) full actuation stress vs. actuation strain diagram, b) detailed view of the area marked in red (for the table of values s. Supporting Table S2). Arrows indicate the strain change direction, i.e., compression and elongation of the SMA wire, during heating and cooling, respectively.

3.2.3. DMTA

The austenite start A_s and austenite finish A_f transformation temperatures determined for each wire configuration are presented in Figure 10. The transformation temperatures for all SMA wire configurations were within the tolerance range specified by the manufacturer (± 10 °C). Also, no significant difference ($p > 0.05$) was found between the SMA wire configurations, suggesting that the electrochemical etching either does not or only minimally affects the transformation temperatures.

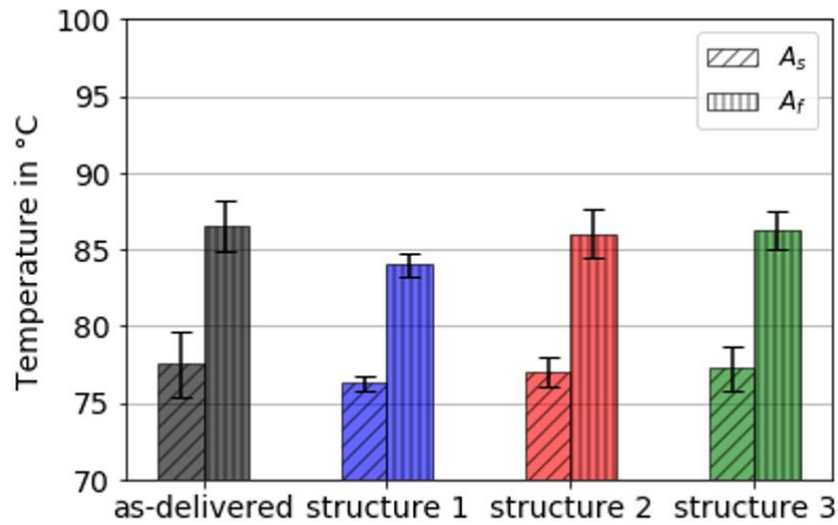


Figure 10. Austenite start A_s and austenite finish A_f transformation temperatures for each wire configuration determined by the DMA test (for the table of values s. Supporting Table S3). Error bars represent standard deviations of the means.

3.3 Pull-Out Test

The pull-out test was performed to measure the maximum shear force transmission between the SMA wire and the polymer matrix. By combining the force-time diagram recorded by the mechanical pull-out testing device with the optical stress measurement, the stress distribution along the SMA wire was examined to determine the first failure at the interface. Figure 11 shows the temporal evolution of the interface failure propagation with increasing pull-out force using structure 2 as an example. The behavior was identical for all SMA wire configurations. At time point (1), the first occurrence of the shear stress at the interface can be observed. At time point (2), the maximum shear stress moved to a different position along the wire, indicating that the interface had already failed at the previous position of the maximum shear stress, long before the failure could be detected from the force-time curve alone. The shear stress continues to

propagate at time point (3) and is then concentrated at a final position (4) before the entire interface fails. Afterwards, only friction effects of the completely debonded SMA wire can be measured during the pull-out. The first failure always occurred at the entry point of the SMA wire into the polymer matrix that can be attributed to the geometry of the pull-out test setup and has already been described elsewhere.⁹

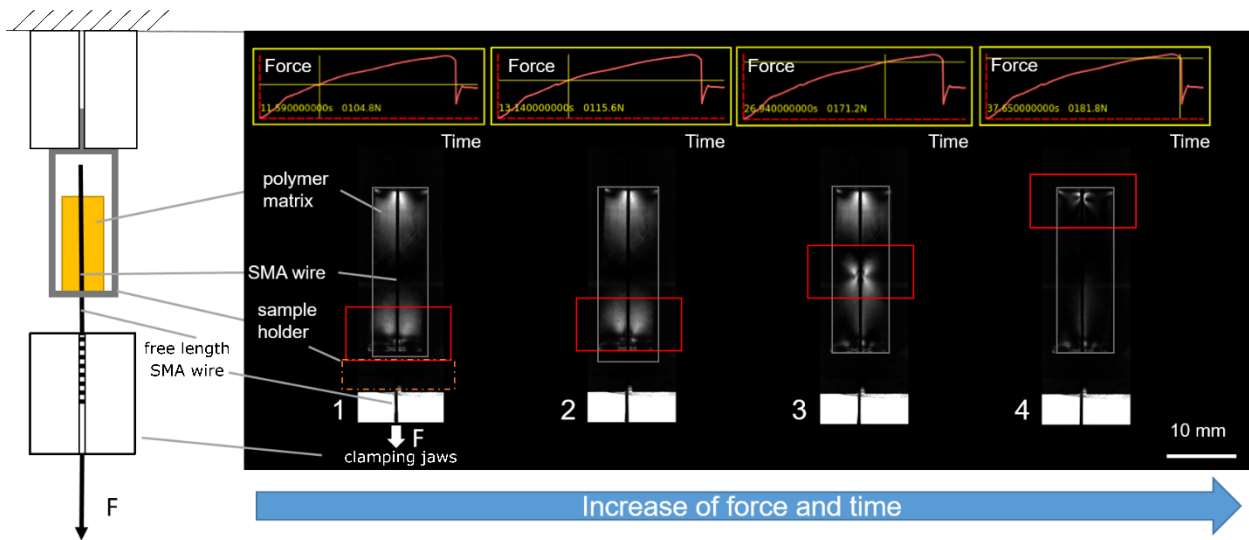


Figure 11. Optical stress measurement during the pull-out test of the SMA wire with structure 2 embedded in the polymer matrix. The maximum shear stress location at each time point (1-4) is marked by the red box, while the sample dimensions are highlighted with the grey box. The corresponding pull-out force is shown in the force-time diagram recorded by the mechanical testing device.

From Figure 12, it can be seen that an approximately 3-fold increase in force transmission in structured SMA wires correlates with an increase in the surface area. Since no chemical bonding occurs between the SMA wire surface and the polymer, this relation indicates that the mechanical interlocking scales with the increase in the surface area. The maximum shear stress at the interface calculated from the force of the first failure according to the analytical model⁵³ is

6.27 MPa for the as-delivered SMA wire and 20.7 MPa for the SMA wire with structure 1. The 3.3-fold increase in the maximum shear stress coincides with the 3.4-fold increase in the surface area of the structured SMA wire.

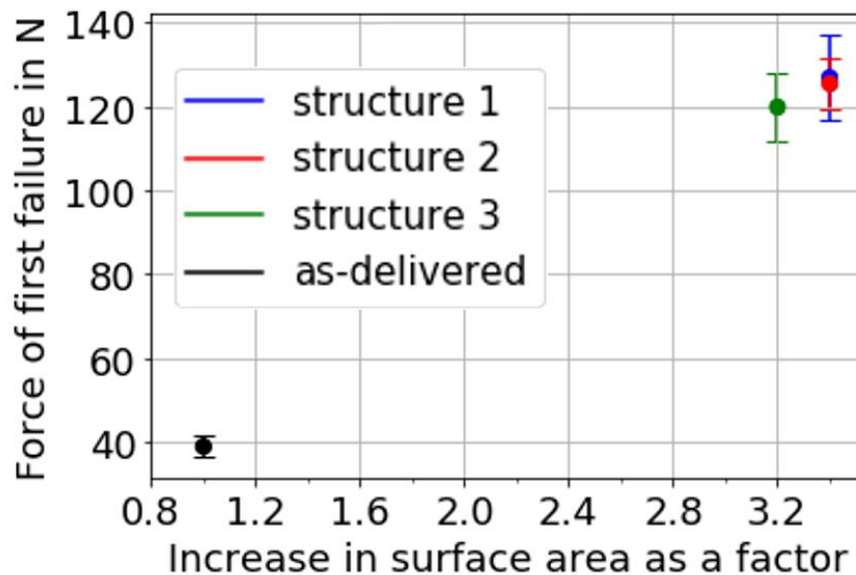


Figure 12. Correlation of the first failure force to the increase in the surface area resulting from electrochemical etching (for the table of values s. Supporting Table S4). Error bars represent standard deviations of the means. Results are shown without outliers.

Considering the standard deviations, no significant difference regarding the force of the first failure between the structured SMA wire configurations could be measured with the present setup. However, the examination of SMA wire surfaces after the pull-out test using SEM (Figure 13) reveals different failure mechanisms for the tested SMA wire configurations. The structure with shallow bowl-like etch pits (structure 3) failed mostly adhesively, while the structures with deeper and partly omega-like etch pits (structure 1 and 2) exhibited a partially cohesive failure showing trapped polymer matrix residuals inside the pits. This indicates that the polymer penetrates into the pits during sample preparation and the force transmission is therefore based

on the mechanical interlocking principle. The as-delivered sample shows almost no polymer matrix residuals on the surface except for the die marks, which originate from the manufacturing process of the SMA wires. The differences in the failure mechanisms for different wire configurations were also confirmed by the investigation of the polymer matrices of the SMA wires after the pull-out test (s. Supporting Figure S5). The polymer matrix of structure 1 exhibited smooth walls since the polymer could not slip out of the deep etch pits, which resulted in a cohesive failure at the interface. In contrast, structure 3 failed mostly adhesively, and the polymer matrix, therefore, showed a "negative" of the wire surface, indicating that the polymer slipped out from the bowl-like flat etch pits.

Distinct differences in failure modes observed for the structured SMA wire configurations also suggest that these structures might perform differently in combination with other polymer matrix materials. The deviations in pull-out results obtained for the structured SMA wires are higher than those for the as-delivered SMA wire. Thereby structure 1 exhibited the highest and structure 2 the lowest standard deviations with 10.2 N and 6.1 N, respectively, while the deviation for the as-delivered SMA wire was 2.4 N. These differences can be attributed to the observed differences in failure modes that range from a purely adhesive failure mode for the as-delivered wire to a combination of adhesive and cohesive failure modes, with the cohesive part being highest for structure 1. Due to the structuring, stress peaks can occur in the polymer matrix at some points, which can be influenced by many parameters such as residual stresses in the polymer matrix, pit shape, and penetration depth of the resin into the pits.

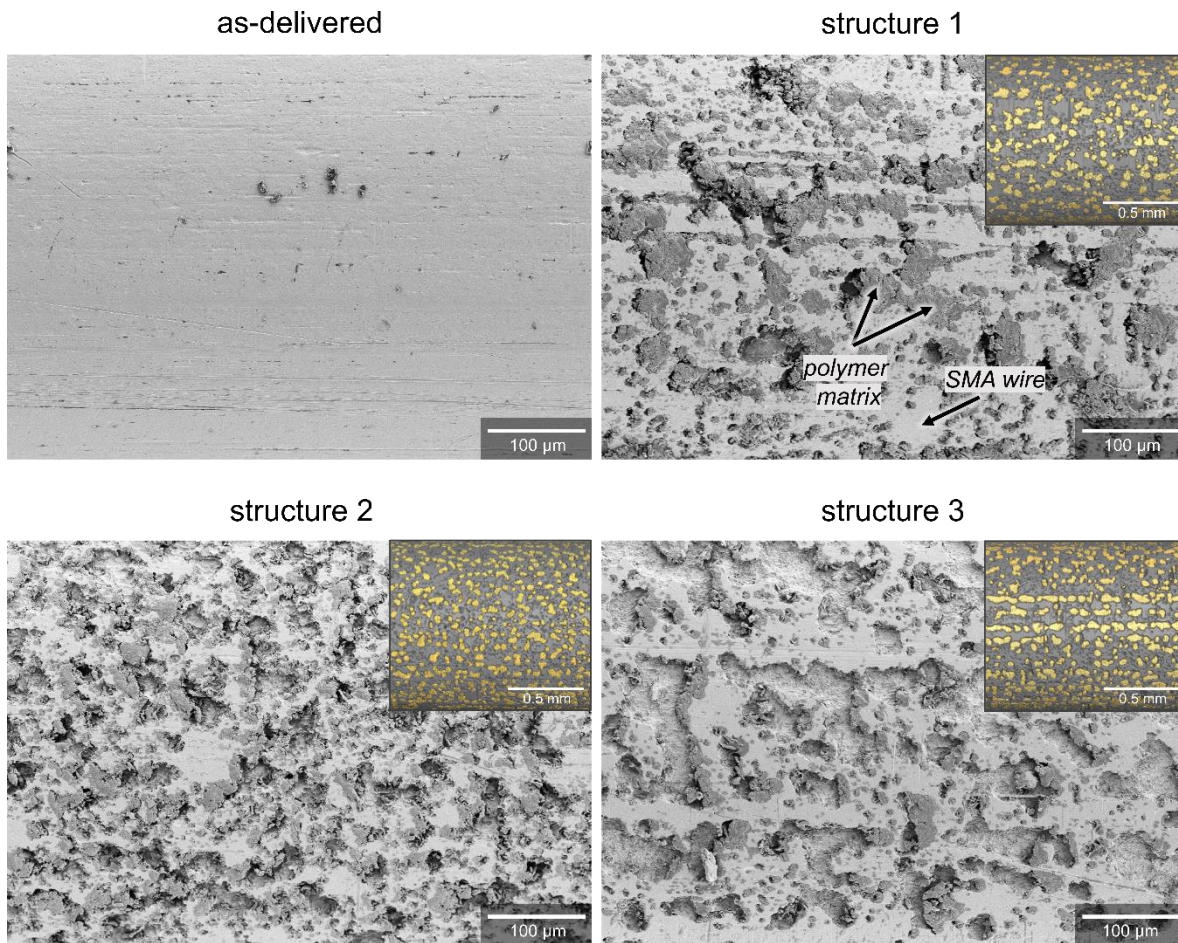


Figure 13. SEM images of the SMA wire surfaces after the pull-out test. In the insets, the corresponding micro-CT images of the original surfaces before the pull-out test are shown.

SUMMARY AND CONCLUSION

This work aimed at increasing the interface adhesion between NiTi SMA wires and the polymer matrix by structuring the wire surface using electrochemical etching. The results can be summarized as follows:

- Three different surface structure morphologies regarding etch pit geometry and pit density were produced by the electrochemical etching process comprising (1) a nucleation step at high current densities and (2) a selective etching step at lower current densities, with the applied current being either pulsed or constant. By pulsing the current, it was possible to enhance the etching selectivity allowing etch pits to grow in depth and form omega-like undercuts. The EDX analysis showed that etched areas are depleted in Ni, indicating that the etching process is selective with respect to Ni.
- Measurement of the maximum force transmission between an SMA wire and the polymer matrix was carried out in pull-out tests combined with an optical stress measurement. The results revealed that the structuring of the SMA wire surface led to an increase in the force of the first failure by more than three times in comparison to as-delivered SMA wires. Investigation of the SMA wire surfaces after the pull-out test revealed different failure mechanisms for the as-delivered (adhesive failure mode) and the structured SMA wires (combined failure modes). The structure with shallow bowl-like etch pits (structure 3) failed mostly adhesively, while the structures with deeper omega-like etch pits (structure 1 and 2) exhibited a partially cohesive failure showing polymer matrix residues within the etch pits. Even though the difference in the force of the first failure between the structured SMA wire configurations was not measurable, distinct differences in failure modes suggest that these structures might perform differently in combination with other polymer matrix materials.
- In mechanical and thermomechanical tests, no significant reduction in the performance behavior of the structured SMA wires was found. All structured SMA wires exhibited the same shape of the stress-strain curves as the as-delivered SMA wire in the pre-

strain, tensile, and actuation tests, indicating that the etching procedure provides a homogeneous structuring along the length of the SMA wire. The actuation characterization test showed that approximately the same work capacity could be retrieved from structured SMA wires. The austenite start A_s and austenite finish A_f transformation temperatures were found not to be affected by the structuring process.

In conclusion, one can state that the structuring of the SMA wire surface by electrochemical etching provides a fast and reproducible method for significant improvement of the interface adhesion without compromising the mechanical and shape memory properties of SMA wires. Thereby an increase in the force of the first failure by more than three times relies on the formation of suitable undercut structures on the SMA wire surface and the mechanical interlocking with the polymer matrix. The structuring process proposed in this work does not lead to hydrogen embrittlement and is selective to crystal defects and impurities. Thus, the etched surface is composed of the most thermodynamically stable surfaces. In addition, no harsh chemicals are required for the process.

Electrochemical etching of two-way effect SMA wires with smaller diameters, thermal activation of hybrid composites composed of structured SMA wires, as well as investigation of the influence of the structuring process on strain behavior and cycling load will be the scope of future work.

ASSOCIATED CONTENT

Supporting Information

The Supporting Information is available free of charge on the ACS Publications website at DOI:

Additional data include details on micro-CT data analysis, detailed views of the stress-strain diagrams obtained from the pre-strain and tensile tests, tables of calculated values from the actuation characterization test, DMTA test, pull-out test, as well as equations for calculation of the maximum transferable shear stress, results of the reproducibility test, and micro-CT images of the polymer matrices after the pull-out test.

AUTHOR INFORMATION

Corresponding Author

* Anna Gapeeva (ang@tf.uni-kiel.de)

* Dr. Jürgen Carstensen (jc@tf.uni-kiel.de)

Author Contributions

The manuscript was written through contributions of all authors. All authors have given approval to the final version of the manuscript.

Notes

The authors declare no competing financial interest.

ACKNOWLEDGMENT

This research was funded by the German Research Foundation (DFG) (funding code AD 183/23-1) on behalf of the German federal and state governments.

The microtomography data were obtained at the beamline HEMS / PETRA III at DESY within the beamtime ID 11010138.

The support of Dr. David Scheliga and Dipl.-Ing. (FH) Jörg Bahr is highly appreciated.

REFERENCES

- (1) Šittner, P.; Stalmans, R. Developing Hybrid Polymer Composites with Embedded Shape-Memory Alloy Wires. *JOM* **2000**, *52* (10), 15–20. <https://doi.org/10.1007/s11837-000-0077-1>.
- (2) Gurka, M. *The Physics of Multifunctional Materials: Concepts, Materials, Applications*; DEStech Publications, Inc.: Lancaster, Pennsylvania, 2018.
- (3) Lagoudas, D. C. *Shape Memory Alloys: Modeling and Engineering Applications*; Springer Science+Business Media, LLC: New York, 2010. <https://doi.org/10.1007/978-0-387-47685-8>.
- (4) Nissle, S.; Kaiser, M.; Hübler, M.; Gurka, M.; Breuer, U. Adaptive Vortex Generators Based on Active Hybrid Composites: From Idea to Flight Test. *CEAS Aeronaut. J.* **2018**, *9* (4), 661–670. <https://doi.org/10.1007/s13272-018-0316-1>.
- (5) Hübler, M.; Weber, L.; Nissle, S.; Gurka, M. Bending Actuator Comprising Shape Memory Element. US Patent 15/567,859, 2018.
- (6) Faiella, G.; Antonucci, V.; Daghia, F.; Fascia, S.; Giordano, M. Fabrication and Thermo-Mechanical Characterization of a Shape Memory Alloy Hybrid Composite. *J. Intell. Mater. Syst. Struct.* **2011**, *22* (3), 245–252. <https://doi.org/10.1177/1045389X10396954>.
- (7) Baitab, D. M.; Majid, D. L. A. H. A.; Abdullah, E. J.; Hamid, M. F. A. A Review of Techniques for Embedding Shape Memory Alloy (SMA) Wires in Smart Woven Composites. *Int. J. Eng. Technol.* **2018**, *7* (4.13), 129–136. <https://doi.org/10.14419/ijet.v7i4.13.21344>.

- (8) Hübler, M.; Gurka, M.; Schmeer, S.; Breuer, U. P. Performance Range of SMA Actuator Wires and SMA-FRP Structure in Terms of Manufacturing, Modeling and Actuation. *Smart Mater. Struct.* **2013**, *22* (9), 094002. <https://doi.org/10.1088/0964-1726/22/9/094002>.
- (9) Nissle, S.; Gurka, M. Characterization of Active Hybrid Structures Made of Fiber Reinforced Composites and Shape Memory Alloys-Part A: Characterization of the Load Transfer. *Smart Mater. Struct.* **2019**, *28* (4), 045002. <https://doi.org/10.1088/1361-665X/ab04db>.
- (10) Wang, Y.; Zhou, L.; Wang, Z.; Huang, H.; Ye, L. Stress Distributions in Single Shape Memory Alloy Fiber Composites. *Mater. Des.* **2011**, *32* (7), 3783–3789. <https://doi.org/10.1016/j.matdes.2011.03.039>.
- (11) Paine, J.; Jones, W.; Rogers, C. Nitinol Actuator to Host Composite Interfacial Adhesion in Adaptive Hybrid Composites. In *33rd Structures. Structural Dynamics and Materials Conference*; 1992; p 2405. <https://doi.org/10.2514/6.1992-2405>.
- (12) Gabry, B.; Thiebaud, F.; Lexcellent, C. Topographic Study of Shape Memory Alloy Wires Used as Actuators in Smart Materials. *J. Intell. Mater. Syst. Struct.* **2000**, *11* (8), 592–603. <https://doi.org/10.1106/XA96-8NV4-DBQ1-2C8G>.
- (13) Poon, C.; Lau, K.; Zhou, L. Design of Pull-out Stresses for Prestrained SMA Wire/Polymer Hybrid Composites. *Compos. Part B Eng.* **2005**, *36* (1), 25–31. <https://doi.org/10.1016/j.compositesb.2004.04.002>.
- (14) Payandeh, Y.; Meraghni, F.; Patoor, E.; Eberhardt, A. Debonding Initiation in a NiTi Shape Memory Wire-Epoxy Matrix Composite. Influence of Martensitic Transformation. *Mater.*

- Des.* **2010**, 31 (3), 1077–1084. <https://doi.org/10.1016/j.matdes.2009.09.048>.
- (15) Jonnalagadda, K.; Kline, G. E.; Sottos, N. R. Local Displacements and Load Transfer in Shape Memory Alloy Composites. *Exp. Mech.* **1997**, 37 (1), 78–86. <https://doi.org/10.1007/BF02328753>.
- (16) Samal, S.; Tyc, O.; Heller, L.; Šittner, P.; Malik, M.; Poddar, P.; Catauro, M.; Blanco, I. Study of Interfacial Adhesion between Nickel-Titanium Shape Memory Alloy and a Polymer Matrix by Laser Surface Pattern. *Appl. Sci.* **2020**, 10 (6), 2172. <https://doi.org/10.3390/app10062172>.
- (17) Lau, K.; Tam, W.; Meng, X.; Zhou, L. Morphological Study on Twisted NiTi Wires for Smart Composite Systems. *Mater. Lett.* **2002**, 57 (2), 364–368. [https://doi.org/10.1016/S0167-577X\(02\)00793-0](https://doi.org/10.1016/S0167-577X(02)00793-0).
- (18) Smith, N. A.; Antoun, G. G.; Ellis, A. B.; Crone, W. C. Improved Adhesion between Nickel-Titanium Shape Memory Alloy and a Polymer Matrix via Silane Coupling Agents. *Compos. Part A Appl. Sci. Manuf.* **2004**, 35 (11), 1307–1312. <https://doi.org/10.1016/j.compositesa.2004.03.025>.
- (19) Merlin, M.; Scoponi, M.; Soffritti, C.; Fortini, A.; Rizzoni, R.; Garagnani, G. L. On the Improved Adhesion of NiTi Wires Embedded in Polyester and Vinylester Resins. *Frat. ed Integrita Strutt.* **2015**, 9 (31), 127–137. <https://doi.org/10.3221/IGF-ESIS.31.10>.
- (20) Kemtchou, S. Y. *Optimierung Der Grenzflächenhaftung Bei NiTi, Polymer- Verbunden Durch Einsatz Funktioneller Zwischenschichten*; Cuvillier: Göttingen, 2008.
- (21) Wang, Y.; Wang, Z.; Zhou, L.; Huang, H. Influence of Silane Coupling Agent on Interfacial

- Strength of SMA Composite. *Adv. Mater. Res.* **2011**, 143–144, 933–937.
<https://doi.org/10.4028/www.scientific.net/AMR.143-144.933>.
- (22) Neuking, K.; Abu-Zarifa, A.; Eggeler, G. Surface Engineering of Shape Memory Alloy/Polymer-Composites: Improvement of the Adhesion between Polymers and Pseudoelastic Shape Memory Alloys. *Mater. Sci. Eng. A* **2008**, 481–482, 606–611.
<https://doi.org/10.1016/j.msea.2007.05.118>.
- (23) Antico, F. C.; Zavattieri, P. D.; Hector, L. G.; Mance, A.; Rodgers, W. R.; Okonski, D. A. Adhesion of Nickel-titanium Shape Memory Alloy Wires to Thermoplastic Materials: Theory and Experiments. *Smart Mater. Struct.* **2012**, 21 (3), 035022.
<https://doi.org/10.1088/0964-1726/21/3/035022>.
- (24) Gomes da Silva, G. T.; Nobre Dantas Grassi, E.; de Amorim, W. F.; de Araújo, C. J. Pull-out Resistance of Shape Memory Alloy Nickel-Titanium Ribbons Embedded in Silicone Matrix for Development of Flexible Composites. *J. Intell. Mater. Syst. Struct.* **2021**, 32 (4), 430–441. <https://doi.org/10.1177/1045389X20957106>.
- (25) Gharbi, O.; Thomas, S.; Smith, C.; Birbilis, N. Chromate Replacement: What Does the Future Hold? *npj Mater. Degrad.* **2018**, 2 (1), 12. <https://doi.org/10.1038/s41529-018-0034-5>.
- (26) Bierwagen, G.; Brown, R.; Battocchi, D.; Hayes, S. Active Metal-Based Corrosion Protective Coating Systems for Aircraft Requiring No-Chromate Pretreatment. *Prog. Org. Coatings* **2010**, 68 (1–2), 48–61. <https://doi.org/10.1016/j.porgcoat.2009.10.031>.
- (27) Baytekin-Gerngross, M.; Gerngross, M. D.; Carstensen, J.; Adelung, R. Making Metal

- Surfaces Strong, Resistant, and Multifunctional by Nanoscale-Sculpturing. *Nanoscale Horizons* **2016**, *1* (6), 467–472. <https://doi.org/10.1039/c6nh00140h>.
- (28) Baytekin-Gerngross, M.; Gerngross, M.-D.; Carstensen, J.; Adelung, R. Chemical Sculpturing of Al Micro-Particles for Polymer Composites and Universal Polymer-Polymer Joints. *ECS Trans.* **2016**, *75* (1), 113–122. <https://doi.org/10.1149/07501.0113ecst>.
- (29) Gerngross, M.-D.; Baytekin-Gerngross, M.; Carstensen, J.; Adelung, R. Self-Organized Growth of Crystallographic Macropores in Multicrystalline Zn by Nanoscale Sculpturing. *J. Electrochem. Soc.* **2018**, *165* (4), H3099–H3106. <https://doi.org/10.1149/2.0141804jes>.
- (30) Kalu, C. O.; Hoppe, M.; Hölken, I.; Baytekin-Gerngross, M.; Gerngross, M. D.; Carstensen, J.; Adelung, R. Formation of Micro-Mechanical Interlocking Sites by Nanoscale Sculpturing for Composites or Hybrid Materials with Stainless Steel. *J. Mater. Res.* **2020**, *35* (23–24), 3145–3156. <https://doi.org/10.1557/jmr.2020.284>.
- (31) Jang, B. K.; Kishi, T. Adhesive Strength between TiNi Fibers Embedded in CFRP Composites. *Mater. Lett.* **2005**, *59* (11), 1338–1341. <https://doi.org/10.1016/j.matlet.2005.01.006>.
- (32) Rossi, S.; Deflorian, F.; Pegoretti, A.; D’Orazio, D.; Gialanella, S. Chemical and Mechanical Treatments to Improve the Surface Properties of Shape Memory NiTi Wires. *Surf. Coatings Technol.* **2008**, *202* (10), 2214–2222. <https://doi.org/10.1016/j.surfcoat.2007.09.013>.
- (33) Zhao, L. M.; Feng, X.; Mi, X. J.; Li, Y. F.; Xie, H. F.; Yin, X. Q. The Interfacial Strength Improvement of SMA Composite Using ZnO with Electrochemical Deposition Method.

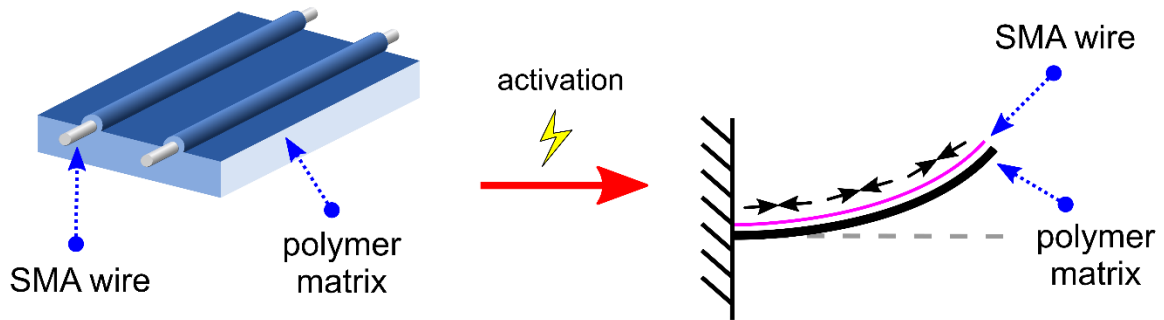
- Appl. Surf. Sci.* **2014**, *320*, 670–673. <https://doi.org/10.1016/j.apsusc.2014.09.125>.
- (34) Zhang, Y.; Mi, C. Strengthening Bonding Strength in NiTi SMA Fiber-Reinforced Polymer Composites through Acid Immersion and Nanosilica Coating. *Compos. Struct.* **2020**, *239*, 112001. <https://doi.org/10.1016/j.compstruct.2020.112001>.
- (35) Murkute, V.; Gupta, A.; Thakur, D. G.; Harshe, R.; Joshi, M. Improvisation of Interfacial Bond Strength in Shape Memory Alloy Hybrid Polymer Matrix Composites. *Procedia Mater. Sci.* **2014**, *6*, 316–321. <https://doi.org/10.1016/j.mspro.2014.07.040>.
- (36) Nagaoka, A.; Yokoyama, K.; Sakai, J. Evaluation of Hydrogen Absorption Behaviour during Acid Etching for Surface Modification of Commercial Pure Ti, Ti-6Al-4V and Ni-Ti Superelastic Alloys. *Corros. Sci.* **2010**, *52* (4), 1130–1138. <https://doi.org/10.1016/j.corsci.2009.12.029>.
- (37) Shabalovskaya, S.; Anderegg, J.; Van Humbeeck, J. Critical Overview of Nitinol Surfaces and Their Modifications for Medical Applications. *Acta Biomater.* **2008**, *4* (3), 447–467. <https://doi.org/10.1016/j.actbio.2008.01.013>.
- (38) Huang, C.; Xie, Y.; Zhou, L.; Huang, H. Enhanced Surface Roughness and Corrosion Resistance of NiTi Alloy by Anodization in Diluted HF Solution. *Smart Mater. Struct.* **2009**, *18* (2), 024003. <https://doi.org/10.1088/0964-1726/18/2/024003>.
- (39) Cattarin, S.; Guerriero, P.; Musiani, M.; Tuissi, A.; Vázquez-Gómez, L. Electrochemical Etching of NiTi Alloy in a Neutral Fluoride Solution. *J. Electrochem. Soc.* **2009**, *156* (12), C428. <https://doi.org/10.1149/1.3240335>.
- (40) Yang, Z.; Wei, X.; Cao, P.; Gao, W. Surface Modification of Nitinol by Chemical and

- Electrochemical Etching. *Mod. Phys. Lett. B* **2013**, *27* (19), 1341012.
<https://doi.org/10.1142/S0217984913410121>.
- (41) Mineta, T. Electrochemical Etching of a Shape Memory Alloy Using New Electrolyte Solutions. *J. Micromechanics Microengineering* **2004**, *14* (1), 76–80.
<https://doi.org/10.1088/0960-1317/14/1/310>.
- (42) Mineta, T.; Makino, E. Characteristics of the Electrochemical Etching of TiNi Shape Memory Alloy in a LiCl-Ethanol Solution. *J. Micromechanics Microengineering* **2010**, *20* (12), 125012. <https://doi.org/10.1088/0960-1317/20/12/125012>.
- (43) Hang, R.; Liu, Y.; Zhao, L.; Gao, A.; Bai, L.; Huang, X.; Zhang, X.; Tang, B.; Chu, P. K. Fabrication of Ni-Ti-O Nanotube Arrays by Anodization of NiTi Alloy and Their Potential Applications. *Sci. Rep.* **2014**, *4* (1), 7547. <https://doi.org/10.1038/srep07547>.
- (44) Xu, L. D.; Sun, X. Y.; Wan, P.; Sun, X. D.; Wang, Z. Q. Surface Treatment of Interfacial Properties of Shape Memory Alloy Composites. *Mater. Res. Innov.* **2015**, *19*, S5-734-S5-738. <https://doi.org/10.1179/1432891714Z.0000000001184>.
- (45) Huntsman. Araldite® LY 5052 / Aradur® 5052 Datasheet <https://www.swiss-composite.ch/pdf/t-Araldite-LY5052-Aradur5052-e.pdf> (accessed Jan 13, 2021).
- (46) Ehrenstein, G. W. *Mit Kunststoffen Konstruieren*; Hanser: Munich, 2007.
- (47) Arganda-Carreras, I.; Kaynig, V.; Rueden, C.; Eliceiri, K. W.; Schindelin, J.; Cardona, A.; Seung, H. S. Trainable Weka Segmentation: A Machine Learning Tool for Microscopy Pixel Classification. *Bioinformatics* **2017**, *33* (15), 2424–2426.
<https://doi.org/10.1093/bioinformatics/btx180>.

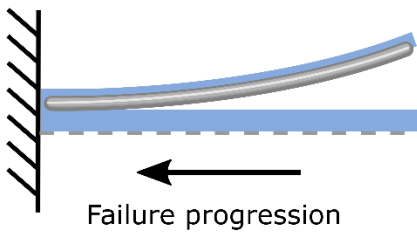
- (48) Hildebrand, T.; Rügsegger, P. A New Method for the Model-Independent Assessment of Thickness in Three-Dimensional Images. *J. Microsc.* **1997**, *185* (1), 67–75. <https://doi.org/10.1046/j.1365-2818.1997.1340694.x>.
- (49) Schindelin, J.; Arganda-Carreras, I.; Frise, E.; Kaynig, V.; Longair, M.; Pietzsch, T.; Preibisch, S.; Rueden, C.; Saalfeld, S.; Schmid, B.; Tinevez, J. Y.; White, D. J.; Hartenstein, V.; Eliceiri, K.; Tomancak, P.; Cardona, A. Fiji: An Open-Source Platform for Biological-Image Analysis. *Nat. Methods* **2012**, *9* (7), 676–682. <https://doi.org/10.1038/nmeth.2019>.
- (50) Fathi, H.; Shokrieh, M. M.; Saeedi, A. Effect of Tensile Loading Rate on Interfacial Properties of SMA/Polymer Composites. *Compos. Part B Eng.* **2020**, *183*, 107730. <https://doi.org/10.1016/j.compositesb.2019.107730>.
- (51) Hübler, M.; Gurka, M.; Breuer, U. P. From Attached Shape Memory Alloy Wires to Integrated Active Elements, a Small Step? Impact of Local Effects on Direct Integration in Fiber Reinforced Plastics. *J. Compos. Mater.* **2015**, *49* (15), 1895–1905. <https://doi.org/10.1177/0021998314550494>.
- (52) Kaiser, R. E.; Mühlbauer, J. A. *Elementare Tests Zur Beurteilung von Meßdaten. Soforthilfe Für Statistische Tests Mit Wenigen Meßdaten*; Bibliogr. Inst. + Brockha: Mannheim, 1989.
- (53) Greszczuk, L. B. Theoretical Studies of the Mechanics of the Fiber-Matrix Interface in Composites. In *Interfaces in Composites*; ASTM International, 1969; pp 42–58. <https://doi.org/https://doi.org/10.1520/STP44699S>.
- (54) Harris, D. C. *Quantitative Chemical Analysis*; W. H. Freeman and Company: New York, 2007.

- (55) Niinomi, M. *Metals for Biomedical Devices*; Woodhead Publishing: Cambridge, 2019.
<https://doi.org/10.1016/C2017-0-03429-8>.
- (56) Carstensen, J.; Prange, R.; Föll, H. A Model for Current-Voltage Oscillations at the Silicon Electrode and Comparison with Experimental Results. *J. Electrochem. Soc.* **1999**, *146* (3), 1134–1140. <https://doi.org/10.1149/1.1391734>.

Active hybrid composite

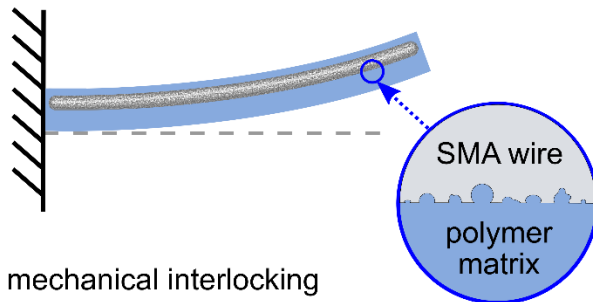


untreated



- ✗ delamination at the interface
- ✗ no force transmission

electrochemically etched



- ✓ mechanical interlocking
- ✓ scaling with surface enlargement
- ✓ most thermodynamically stable surfaces

Supporting Information for

Electrochemical Surface Structuring for Strong SMA Wire – Polymer Interface Adhesion

Anna Gapeeva,^{,†} Julia Vogtmann,[‡] Berit Zeller-Plumhoff,[§] Felix Beckmann,[‡] Martin Gurka,[‡]
Jürgen Carstensen,^{*,†} Rainer Adelung[†]*

[†] Functional Nanomaterials, Institute for Materials Science, Faculty of Engineering, Kiel
University, Kaiserstraße 2, D-24143 Kiel, Germany

[‡] Leibniz Institute for Composite Materials (IVW), Erwin-Schrödinger-Straße 58, D-67663
Kaiserslautern, Germany

[§] Helmholtz-Zentrum Geesthacht, Institute of Metallic Biomaterials, Max-Planck-Straße 1, D-
21502 Geesthacht, Germany

[‡] Helmholtz-Zentrum Geesthacht, Institute of Materials Physics, Max-Planck-Straße 1, D-21502
Geesthacht, Germany

Corresponding Authors

* Anna Gapeeva (ang@tf.uni-kiel.de), * Dr. Jürgen Carstensen (jc@tf.uni-kiel.de)

S1 Separation of pits (micro-CT)

Due to the surface roughness of the SMA wire originating from the nucleation step, deep etch pits created during the selective electrochemical etching step were sometimes identified as one large pit (Figure S.1). To separate the erroneously connected pits, the BoneJ thickness plugin¹ in Fiji ImageJ² was used. Thereby, for each voxel of an etch pit, a sphere was determined, and a minimum value for the spheres was set. Thus, all pits smaller than 15 voxels were excluded, which comprised tiny flat “connection” holes.

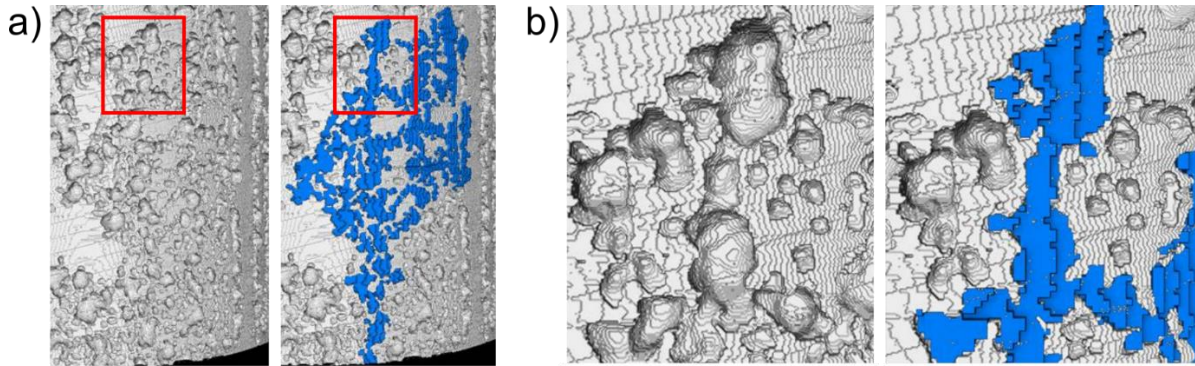


Figure S1. Example of erroneously connected pits: a) full-view of the SMA wire surface (structure 2) and the etched volume identified as one pit (in blue), b) detailed view of the area marked in red.

S2 Calculation of the maximum transferable shear stress

After the pull-out test, the maximum transferable shear stress was calculated according to Greszczuk³ using the following equations (1) and (2):

$$\tau(x) = F_w \frac{\alpha}{2\pi r} [\coth(\alpha L_e) \cosh(\alpha x) - \sinh(\alpha x)] \quad (1)$$

$$\alpha = \sqrt{2\pi \frac{G_m}{\left(\frac{r}{R}\right)} \left(\frac{1}{\pi r^2 E_w} - \frac{1}{\pi R^2 E_m} \right)} \quad (2)$$

where F_w is the force of the first failure at the interface determined during the pull-out test combined with the optical stress measurement, G_m is the shear modulus of the polymer matrix calculated according to Ehrenstein⁴, r is the radius of the SMA wire (derived from the cross-sectional areas determined by micro-CT), and R is the radius of the surrounding polymer matrix, both values were defined by sample dimensions. Taking the radius determined from the measured cross-sectional area results in approx. 1% change in shear stress compared to the assumed radius of 0.5 mm for all wire configurations. E_w is the tensile modulus of the SMA wire, which was measured during pre-straining of the SMA wire. E_m is the tensile modulus of the polymer matrix (datasheet⁵), and L_e is the embedded SMA wire length (defined by sample dimensions).

Table S1. Values used to calculate the maximum shear stress during the pull-out test according to Greszczuk using equations (1) and (2).

Symbol	Used values
F_w : Force of the first failure at the interface [N]	as-delivered: 39 structure 1: 126.9 structure 2: 125.5 structure 3: 119.9
G_m : Shear modulus of the polymer matrix [MPa]	1240.74
r : Radius of the SMA wire [mm]	as-delivered: 0.5069

	structure 1: 0.50215 structure 2: 0.50210 structure 3: 0.50155
R: Radius of the surrounding polymer matrix [mm]	8
E_w : Tensile modulus of the wire [MPa]	12776
E_m : Tensile modulus of the polymer matrix [MPa]	1240.74
L_e : Embedded SMA wire length [mm]	50

S3 Pre-strain and tensile test

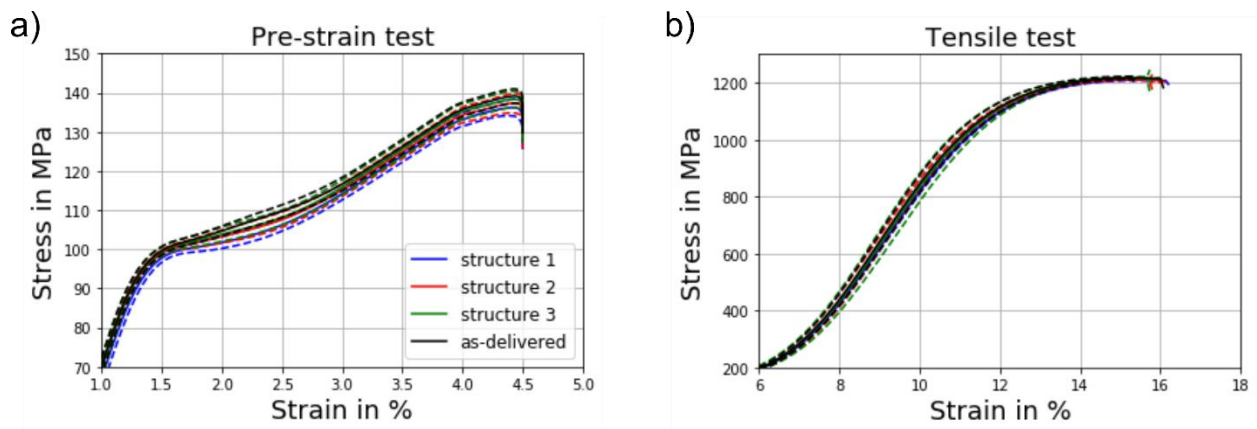


Figure S2. Detailed views of the stress-strain diagrams obtained from a) the pre-strain test, b) the tensile test. Solid lines represent the average stress values, while dotted lines indicate the corresponding 99 % confidence interval.

S4 Reproducibility test

Three SMA wire samples electrochemically etched with structure 1 were analyzed. The samples were scanned (Figure S.4a) using the 3D Laser Scanning Confocal Microscope VK-X (Keyence Corporation, Osaka, Japan). Thereby the etched area of the wire (10 cm) was cut into five pieces of 2 cm length each, and one measurement in the middle of each piece was conducted. The light source was a red semiconductor laser with a wavelength of 658 nm. At each region of investigation, roughness values Ra and Rz were obtained by averaging roughness values along 61 lines (Figure S.4b). The results are presented in Figure S.4c. One-way ANOVA analysis followed by a Tukey test was performed to verify whether the difference between the values obtained for the three samples was significant. The results showed that the difference of the means was not significant at the 0.05 level ($p > 0.05$), indicating good reproducibility of the electrochemical etching process.

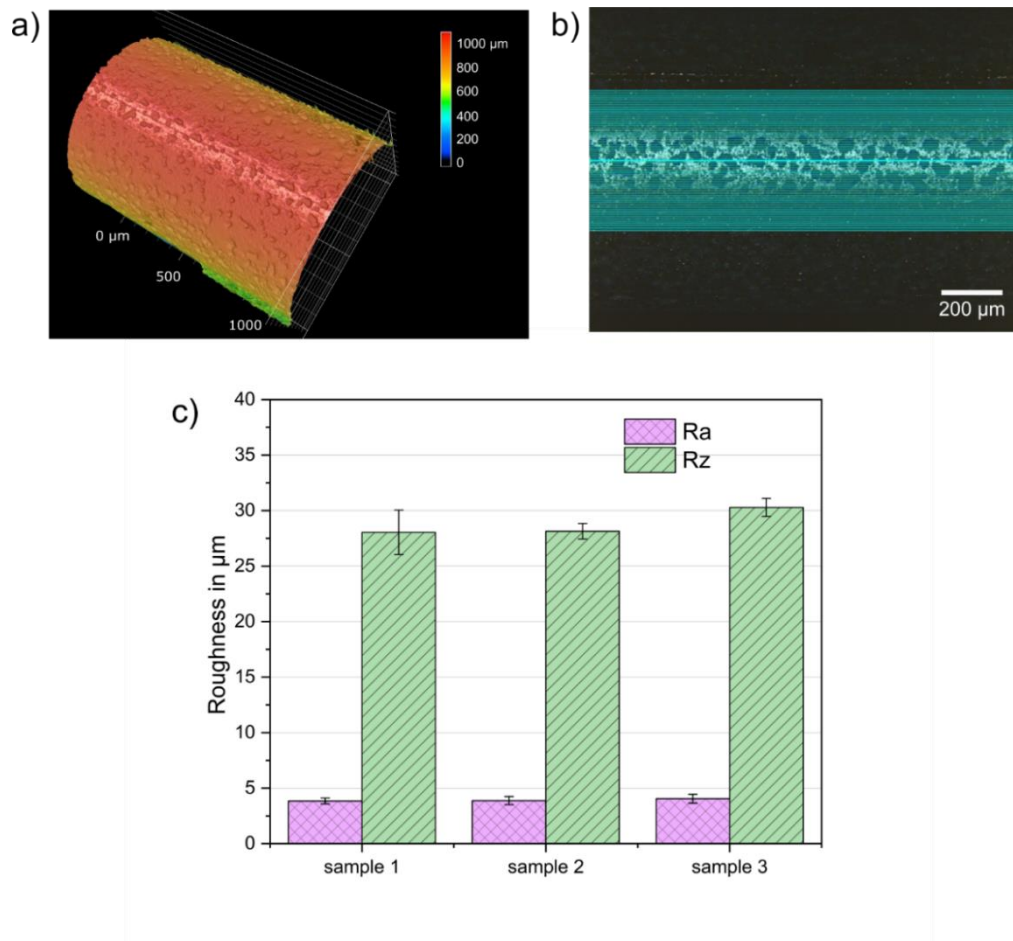


Figure S3. Reproducibility test conducted using confocal microscopy: a) exemplary 3D image after scanning, showing one region of investigation, b) multiple line scans (in blue) for determination of roughness values at one region of investigation (light blue line represents the middle line), c) mean roughness values Ra and Rz with a standard deviation obtained for three samples with structure 1 at five different regions of investigation each.

S5 Actuator characterization test

With the characterization test setup, the SMA wire behavior against an external load can be characterized, giving the first hint about the performance of the SMA wire for actuation purposes. The SMA wire is activated with an electric current, giving rise to Joule heating and the change of

the intrinsic structure in the SMA wire so that the shape memory effect can be measured. The SMA wire contracts and with that works against the spring. After reaching the maximum strain, the SMA wire remains at the same strain level during heating. When the electric current is switched off, the SMA wire cools down due to the air convection. The spring pre-strained the SMA wire again after the martensite start temperature M_s was reached. Due to the switch-off criterion of the characterization test, the test was aborted earlier in the case of the as-delivered SMA wire, which explains the differences in the SMA wires' recovery behavior in the stress-strain diagram.

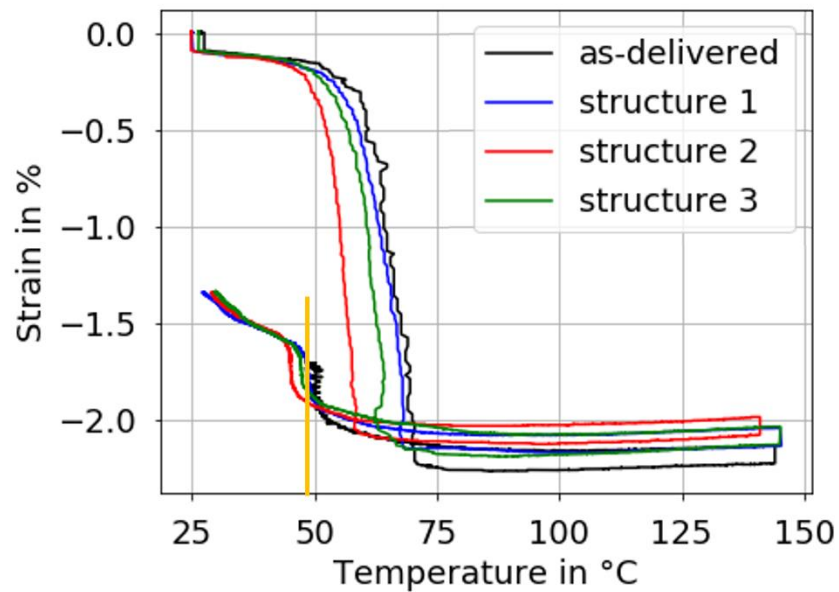


Figure S4. Strain-temperature diagram, showing the temperature-controlled strain behavior of the SMA wires. The yellow line marks the point where the characterization test of the as-delivered SMA wire was interrupted.

Table S2 Results from the actuation characterization test.

	structure 1	structure 2	structure 3	as-delivered
Maximum stress [MPa]	118.6	116.7	123.9	122.2
Maximum strain [%]	-2.168	-2.124	-2.189	-2.265
Work capacity from pre-straining [J]	0.437	0.440	0.443	0.455
Work capacity from actuation [J]	0.233	0.225	0.248	0.255
Work capacity retrieved [%]	53.3	58	57.3	56

S6 DMTA

Table S3. Results of the DMTA, showing the calculated mean values with the corresponding confidence intervals for all tested wire configurations.

	structure 1	structure 2	structure 3	as-delivered
Austenite start A_s temperature [°C]	76.2 ± 0.9	77 ± 0.9	77.3 ± 1.7	77.6 ± 1.9
Austenite finish A_f temperature [°C]	84.2 ± 0.8	86 ± 1.5	86.3 ± 1.2	86.5 ± 1.9

S7 Pull-out test

Table S4. Results of the pull-out test, showing the calculated average values with the corresponding confidence intervals for all tested wire configurations.

	structure 1	structure 2	structure 3	as-delivered
Increase in surface area as a factor	3.4 x	3.4 x	3.2 x	1 x
Force of the first failure [N] (4 samples)	126.9 ± 10.2	125.5 ± 6.1	119.9 ± 8.1	39 ± 2.4
Increase in the force of the first failure as a factor	3.3 x	3.2 x	3.1 x	1 x
Maximum shear stress [MPa] according to Greszczuk	20.7	20.6	19.7	6.27

After the pull-out test, the remaining polymer matrices were imaged with the Nanotom micro-CT (Phoenix X-ray Systems & Services GmbH, Wunstorf, Germany). The chosen photon energy was 90 keV and the imaging was performed around 360° with 2400 projections. A voxel size of 6 µm and an exposure time of 500 ms were selected. Reconstruction was made with a corresponding reconstruction software from Phoenix (pca reconstructor) and VGStudio Max 3.2.2 (Volume Graphics GmbH, Heidelberg, Germany).

The differences in the failure mechanisms for different wire configurations (described in Section 3.3) were confirmed by the investigation of the polymer matrices after the SMA wires were pulled-out (Figure S.7). Structure 1 exhibited combined failure modes, with the cohesive part being attributed to the deep omega-like etch pits, from which the polymer could not slip out, resulting in a smooth wall of the polymer matrix. In contrast, structure 3 failed mostly adhesively, and the

polymer matrix, therefore, shows a “negative” of the wire surface, indicating that the polymer slipped out from the bowl-like flat etch pits.

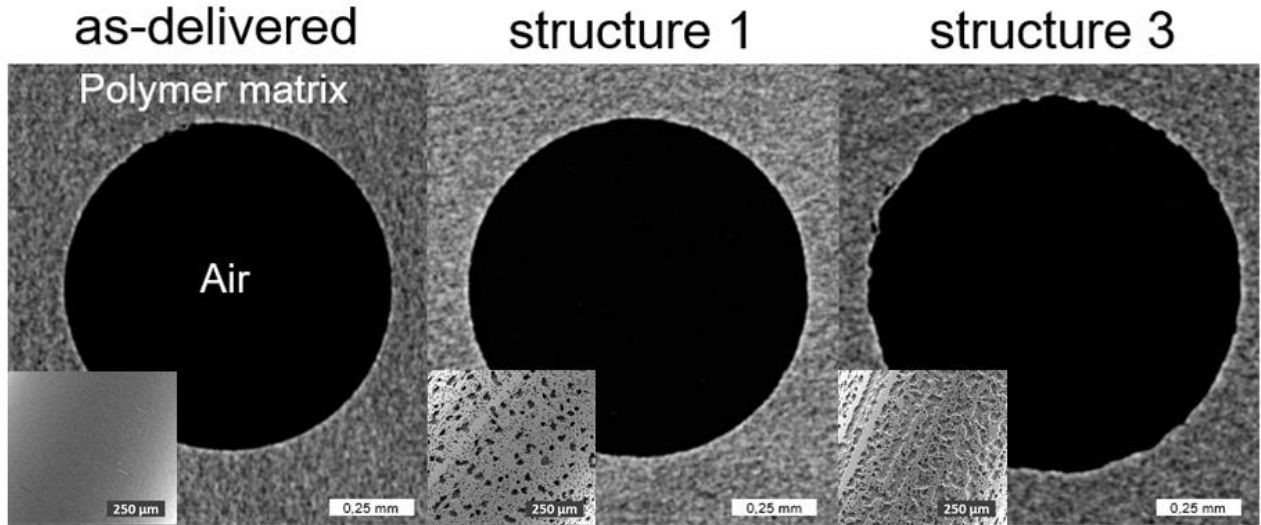


Figure S5. Polymer matrices after the SMA wires were pulled out.

REFERENCES

- (1) Hildebrand, T.; Rügsegger, P. A New Method for the Model-Independent Assessment of Thickness in Three-Dimensional Images. *J. Microsc.* **1997**, *185* (1), 67–75. <https://doi.org/10.1046/j.1365-2818.1997.1340694.x>.
- (2) Schindelin, J.; Arganda-Carreras, I.; Frise, E.; Kaynig, V.; Longair, M.; Pietzsch, T.; Preibisch, S.; Rueden, C.; Saalfeld, S.; Schmid, B.; Tinevez, J. Y.; White, D. J.; Hartenstein, V.; Eliceiri, K.; Tomancak, P.; Cardona, A. Fiji: An Open-Source Platform for Biological-Image Analysis. *Nat. Methods* **2012**, *9* (7), 676–682. <https://doi.org/10.1038/nmeth.2019>.
- (3) Greszczuk, L. B. Theoretical Studies of the Mechanics of the Fiber-Matrix Interface in Composites. In *Interfaces in Composites*; ASTM International, 1969; pp 42–58. <https://doi.org/https://doi.org/10.1520/STP44699S>.

- (4) Ehrenstein, G. W. *Mit Kunststoffen Konstruieren*; Hanser: Munich, 2007.
- (5) Huntsman. Araldite® LY 5052 / Aradur® 5052 Datasheet <https://www.swiss-composite.ch/pdf/t-Araldite-LY5052-Aradur5052-e.pdf> (accessed Jan 13, 2021).